Ground Deformations in the Corinth Rift, Greece, Investigated Through the Means of SAR Multitemporal Interferometry

Panagiotis Elias, Pierre Briole

▶ **To cite this version:**

Panagiotis Elias, Pierre Briole. Ground Deformations in the Corinth Rift, Greece, Investigated Through the Means of SAR Multitemporal Interferometry. Geochemistry, Geophysics, Geosystems, 2018, 19 (12), pp.4836-4857. 10.1029/2018GC007574 . hal-02293260

HAL Id: hal-02293260
https://hal.science/hal-02293260

Submitted on 20 Sep 2019

HAL is a multi-disciplinary open access archive for the deposit and dissemination of scientific research documents, whether they are published or not. The documents may come from teaching and research institutions in France or abroad, or from public or private research centers.

L'archive ouverte pluridisciplinaire **HAL**, est destinée au dépôt et à la diffusion de documents scientifiques de niveau recherche, publiés ou non, émanant des établissements d'enseignement et de recherche français ou étrangers, des laboratoires publics ou privés.

AGU100 ADVANCING EARTH AND SPACE SCIENCE

Geochemistry, Geophysics, Geosystems

RESEARCH ARTICLE
10.1029/2018GC007574

Key Points:
- PSInSAR is combined with GPS to calculate vertical and east-west ground deformation rate maps of the Corinth rift for the period 2002 to 2010
- Several deformed zones are detected, quantified, classified and discussed; they are of deltaic and urban subsidence, and tectonic origin
- Aigion's fault shallow part is slow slipping due to postseismic relaxation; the Rio-Patras fault is locked at shallows and creep at depth

Supporting Information:
- Supporting Information S1
- Table S1
- Table S2
- Figure S1
- Figure S2
- Figure S3
- Figure S4

Correspondence to:
P. Elias,
pelias@noa.gr

Citation:
Elias, P., & Briole, P. (2018). Ground deformations in the Corinth rift, Greece, investigated through the means of SAR multitemporal interferometry. *Geochemistry, Geophysics, Geosystems*, *19*, 4836–4857. https://doi.org/10.1029/2018GC007574

Received 27 MAR 2018
Accepted 6 NOV 2018
Accepted article online 8 NOV 2018
Published online 3 DEC 2018

©2018. American Geophysical Union. All Rights Reserved.

Ground Deformations in the Corinth Rift, Greece, Investigated Through the Means of SAR Multitemporal Interferometry

P. Elias[1] and **P. Briole**[2]

[1]Institute for Astronomy, Astrophysics, Space Applications and Remote Sensing, National Observatory of Athens, Penteli, Greece, [2]Laboratoire de Géologie, UMR CNRS 8538, Ecole Normale Supérieure, PSL Research University, Paris, France

Abstract The Corinth Rift is one of the narrowest and fastest extending continental regions worldwide and has one of the highest seismicity rates in the Euro-Mediterranean region. At its western termination, several active faults are located beneath the city of Patras and the surrounding area, a region of major socioeconomic importance for Greece. Displacement rates for the period 2002–2010 obtained from ascending and descending ASAR/ENVISAT multitemporal interferometry are combined with Global Positioning System measurements from permanent and campaign stations to produce a map of vertical and east-west ground velocities. Cross sections are produced in order to quantify the deformation rates with higher precision. In the vertical, the motion combines tectonic deformation, urban subsidence, and subsidence due to deltaic sediments compaction. In the city of Patras and through the gulf of Patras, the northern continuation of the 2008 Movri earthquake fault is connected to the oblique transform zone of Rio. Further east, our observations suggest the existence of postseismic deformation at Aigion in the 15 years following the M_w = 6.2, 15 June 1995 Aigion earthquake. The inferred deforming zone, assuming a simple slow slipping model, is located at the western end of the 1995 fault, with radius ~3.5 km, centroid depth ~4 km, and cumulated postseismic moment representing 28% of the coseismic. Alluvial fan deltas subside due to their compaction with a gradient that increases toward the shore. Several of those deltas are located in the hanging-wall of active faults.

Plain Language Summary The Gulf of Corinth, Greece, is a seismic area. Apart from moderate earthquakes striking often, additional geological phenomena, such as slow and continuous ground displacements, are occurring. Both are being induced by the movement of the tectonic plates. In many cases slow displacements are part of the seismic cycle occurring before an earthquake. The coast of Central Greece is moving away from the coast of northern Peloponnesus with a maximum velocity of about 1.5 cm per year. This study assesses the land displacements occurring due to tectonic activity of the area. This information is important to evaluate the seismic hazard and its impact on the socioeconomical activity of the region. Continuous ground displacements not associated to large earthquakes in the analyzed period are localized in the city of Patras, Rio, Aigion, and also in the surrounding areas. In the Mornos, near Patras and several other deltas, subsidence of no tectonic origin is detected. The maintenance and the expansion of the ground network are crucial for the uninterrupted monitoring of the geological phenomena. Our study can contribute to the awareness of the civilians, local authorities, and the state.

1. Introduction

The rift of Corinth, Greece (Figure 1), is among the fastest extending continental regions in the world. It is bounded on both sides by active normal faults, onshore and offshore (Moretti et al., 2003; Palyvos et al., 2007) with cumulated offset ~3 km and a series of tilted blocks along the south coast (Doutsos & Poulimenos, 1992; Koukouvelas et al., 1999). It has one of the highest seismicity rates in the Euro-Mediterranean region with, on average, one $M_w > 6$ earthquake per decade. Recent large earthquakes include Alkyonides 1981 (M = 6.7), Galaxidi 1992 (M_w = 5.8), Aigion 1995 (M_w = 6.1), and Movri 2008 (M_w = 6.4). This last event is located outside of the rift, but is connected to it and is crucial for deciphering the deformation processes at the western termination of the rift and its junction with the Gulf of Patras.

The extension across the rift increases from east to west (Avallone et al., 2004) where the current microseismicity (Figure 2) is the highest with large active faults, for example, the Rio-Patras fault zone, the Psathopyrgos fault, the Aigion-Neos-Erineos-Lambiri fault zone, and the Helike fault, onshore and offshore fault systems (Palyvos et al., 2005, 2007). The western termination of the rift is populated with several

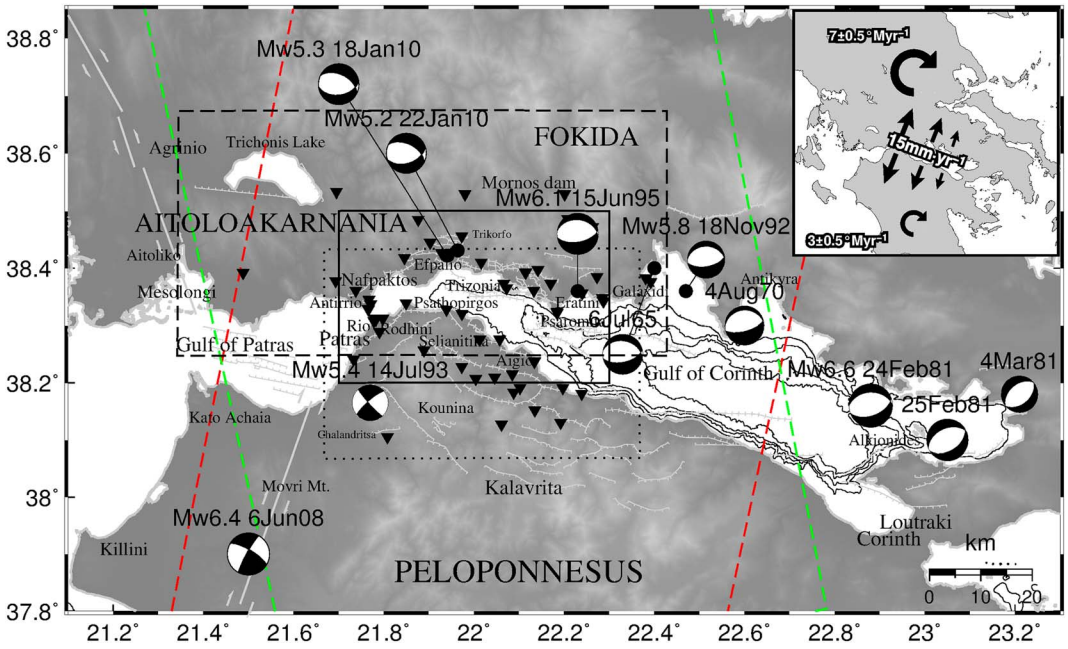

Figure 1. Major earthquakes in the last ~50 years in and around the Corinth rift. Focal mechanisms are from Serpetsidaki et al. (2014), Sokos et al. (2012), Kiratzi and Louvari (2003), Baker et al. (1997), Bernard et al. (1997), Braunmiller and Nábělek (1996), Hatzfeld et al. (1996), Taymaz et al. (1991), Liotier (1989), and Papazachos (1975). Faults traces, originally from Flotte et al. (2005), were compiled during the EU project SISCOR (http://siscor.crlab.eu), using in particular Moretti et al. (2003), Palyvos et al. (2005), and Bell et al. (2008). Red and green dashed lines show the swaths of the ascending track 415 and descending track 279, respectively. Reversed black triangles show the locations of the GPS sites used in the study. The dashed box shows the studied area (see Figure 2). The solid and the dotted box delimit the north and the south *view*, respectively.

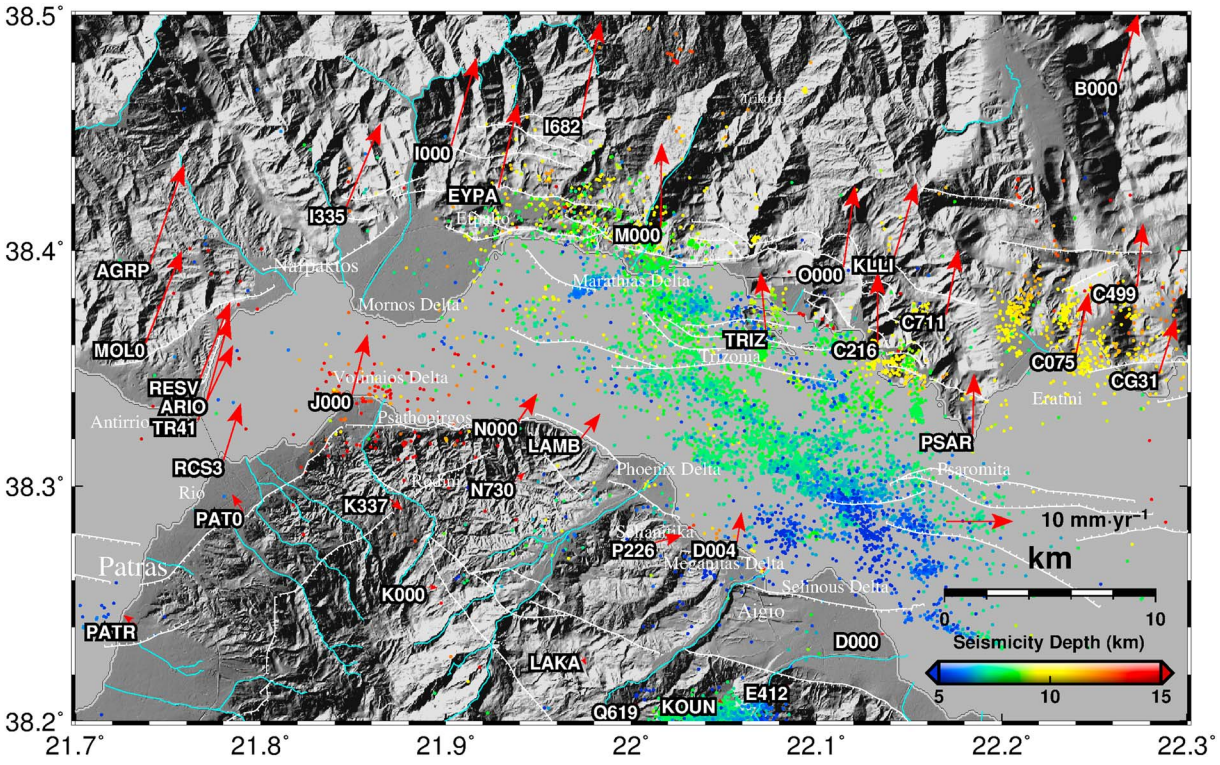

Figure 2. Shaded topography of the western Gulf of Corinth. Relocated seismicity from Lambotte et al. (2014). GPS velocity vectors and corresponding names from Avallone et al. (2004) and Briole et al. (2000), updated. RAb = Rio-Antirio bridge.

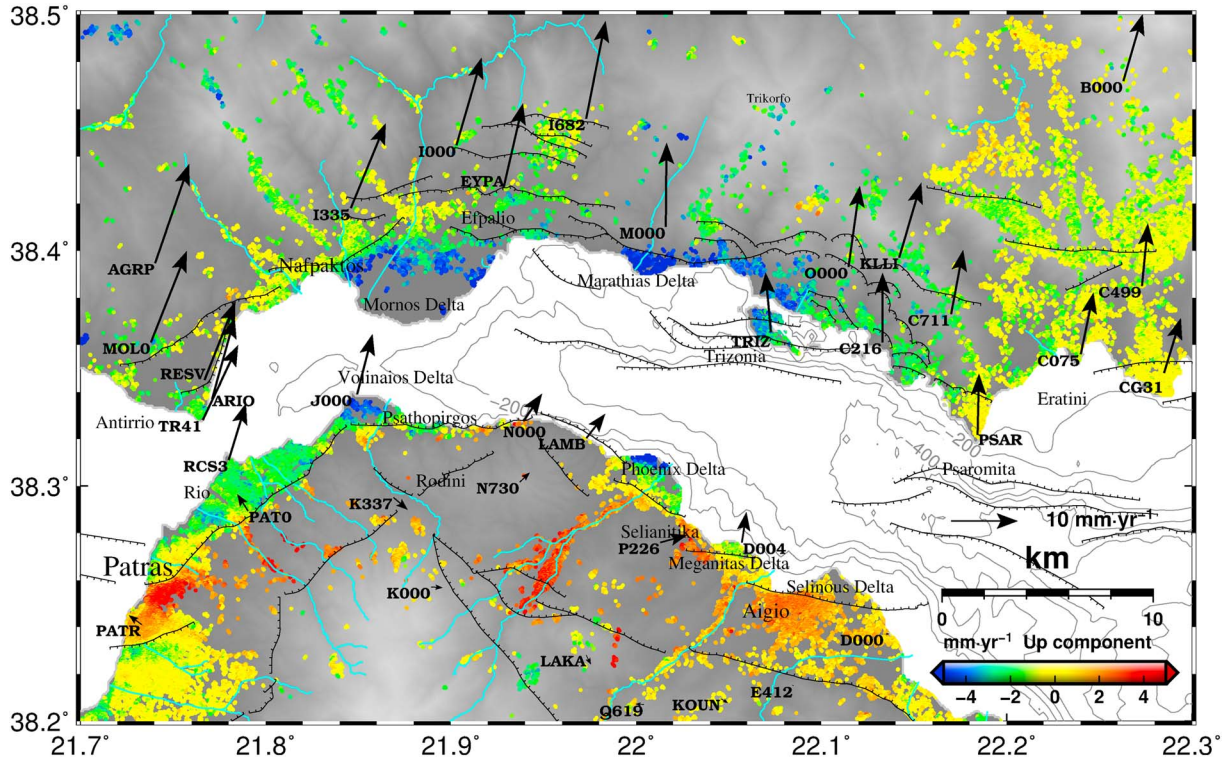

Figure 3. Vertical velocities map from the combination of ascending and descending views. Black lines indicate the faults. The velocity vectors and the names of the GPS points are shown.

towns, among them is the city of Patras, the third largest city in Greece. Major infrastructure are located close to the active faults, for example, the Rio-Antirio bridge linking Peloponnesus to the eastern mainland, the Mornos dam (Figure 1) with its reservoir that supplies water to Athens, the highway and railway connecting Patras to Athens.

On the Psathopyrgos fault, the westernmost major fault, close to Patras, the uplifted terraces suggest four events in the last 2000 years (Palyvos et al., 2007), thus an average recurrence time of earthquakes of ~500 years. As it has not produced significant earthquake for more than 400 years, this fault is considered as a major threat today. To the west, the Rio-Patras fault is a transfer fault zone between the Corinth rift and the normal faults inferred offshore in the southern gulf of Patras (Flotte et al., 2005). It is admitted (e.g., Serpetsidaki et al., 2014) that the Rio-Patras fault is the northern segment of a boundary between the *rigid* Peloponnesus and the *Killini block* located to its west (Figure 1), and continues southward with the fault of the 2008 Movri earthquake.

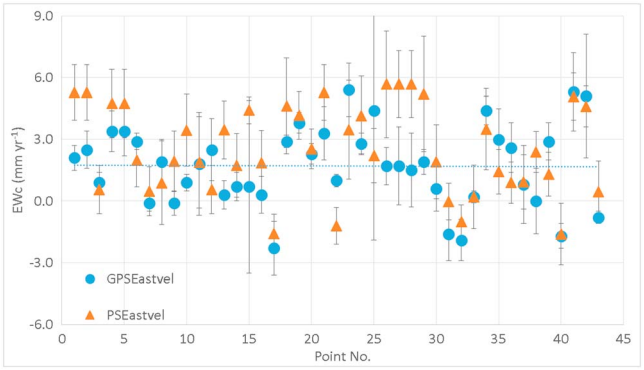

Figure 4. Diagram of the 43 east-west GPS and corresponding PS velocity values and their uncertainties. The numerical values are in Table 1.
PS = Persistent Scatterers.

There are several subaerial and subaqueous deltas (Piper et al., 1990) and fault-controlled Gilbert-type fan deltas (Rohais et al., 2008), with several faults located close to them. In places the prodelta slope is modified by tidal current erosion (Piper et al., 1990).

Using multitemporal synthetic aperture radar interferometry (InSAR), Parcharidis et al. (2009) measured vertical motions in the cities of Patras, Rio, and Antirio, and attribute them primarily to tectonic movements. Geodetic studies based on GPS and InSAR observations gathered in the last 20 years indicate ~NS extension across the rift at a rate reaching 15 mm/year at its western termination across the Pasthopyrgos fault (Avallone, 2003; Avallone et al., 2004; Briole et al., 2000; Clarke et al., 1997).

Table 1
Eastward and Vertical GPS and InSAR Velocity at 43 GPS Points

N	Code	Long (°)	Lat (°)	GPS east (mm/year)	InSAR east (mm/year)	GPS up (mm/year)	InSAR up (mm/year)
1	3000	22.1420	38.3970	2.1 ± 0.6	5.3 ± 1.3		
2	3002	22.1420	38.3970	2.5 ± 0.9	5.3 ± 1.3		
3	3100	22.2850	38.3480	0.9 ± 0.5	0.5 ± 1.2		
4	ARI4	21.7710	38.3370	3.4 ± 1.0	4.7 ± 1.7		
5	ARIO	21.7710	38.3370	3.4 ± 1.2	4.7 ± 1.7		
6	B000	22.2630	38.4720	2.9 ± 0.4	2.0 ± 1.3		
7	C000	22.1840	38.3240	−0.1 ± 0.4	0.5 ± 1.2		
8	C075	22.2400	38.3560	1.9 ± 1.1	0.9 ± 2.0		
9	C131	22.2870	38.3420	−0.1 ± 0.6	1.9 ± 1.5		
10	C499	22.2730	38.3850	0.9 ± 0.4	3.5 ± 1.7		
11	C711	22.1700	38.3730	1.8 ± 2.5	1.9 ± 2.2		
12	CG31	22.2850	38.3480	2.5 ± 1.5	0.5 ± 1.2		
13	CT30	22.3810	38.3830	0.3 ± 0.7	3.5 ± 1.4		
14	D000	22.1340	38.2370	0.7 ± 0.7	1.7 ± 1.5		
15	D004	22.0570	38.2760	0.7 ± 4.2	4.4 ± 0.6		
16	D005	22.1340	38.2380	0.3 ± 0.9	1.9 ± 1.6		
17	DIAK	22.1970	38.1910	−2.3 ± 1.3	−1.6 ± 1.0		
18	EYPA	21.9284	38.4268	2.9 ± 0.3	4.6 ± 2.3	−1.6 ± 0.5	−1.0 ± 0.8
19	I000	21.9029	38.4447	3.8 ± 0.5	4.2 ± 1.2		
20	J000	21.8494	38.3389	2.3 ± 0.5	2.5 ± 1.0		
21	KLLI	22.1420	38.3970	3.3 ± 1.3	5.3 ± 1.3		
22	KOUN	22.0458	38.2095	1.0 ± 0.3	−1.2 ± 0.9	0.0 ± 0.5	0.0 ± 0.5
23	MOL0	21.7380	38.3610	5.4 ± 1.3	3.5 ± 2.4		
24	N000	21.9391	38.3276	2.8 ± 0.5	4.2 ± 1.9		
25	N200	22.2080	38.4860	4.4 ± 6.3	2.2 ± 1.3		
26	O000	22.1146	38.3931	1.7 ± 0.9	5.7 ± 2.6		
27	O002	22.1140	38.3930	1.7 ± 1.9	5.7 ± 1.6		
28	O003	22.1140	38.3930	1.5 ± 1.8	5.7 ± 1.6		
29	O005	22.1150	38.3930	1.9 ± 0.6	5.2 ± 2.8		
30	O106	22.0660	38.3730	0.6 ± 1.1	1.9 ± 1.8		
31	PAT0	21.7905	38.2894	−1.6 ± 1.3	0.0 ± 0.9	−0.7 ± 1.0	−1.1 ± 0.4
32	PATR	21.7330	38.2410	−1.9 ± 1.0	−1.0 ± 0.8		
33	PSAR	22.1843	38.3217	0.2 ± 0.3	0.2 ± 1.5	0.0 ± 0.3	0.2 ± 0.6
34	RC01	21.6933	38.3778	4.4 ± 0.7	3.5 ± 2.0		
35	RCS2	21.7820	38.3120	3.0 ± 1.5	1.4 ± 1.1		
36	RCS3	21.7800	38.3110	2.6 ± 1.2	0.9 ± 1.0		
37	RIO2	21.7780	38.3080	0.8 ± 1.9	0.9 ± 1.3		
38	RIO4	21.7980	38.3120	0.0 ± 1.6	2.4 ± 1.0		
39	RION	21.7827	38.3109	2.9 ± 0.9	1.3 ± 1.1		
40	T000	22.2390	38.1810	−1.7 ± 0.6	−1.6 ± 1.5		
41	TR41	21.7660	38.3280	5.3 ± 1.9	5.1 ± 1.1		
42	TR4A	21.7660	38.3290	5.1 ± 3.0	4.6 ± 1.0		
43	TRIZ	22.0727	38.3654	−0.8 ± 0.3	0.4 ± 1.5	−2.3 ± 0.5	−2.9 ± 0.8

Note. InSAR velocities are computed by averaging the determinations at pixels located within 0.4 km around the GPS point.

Here we analyze the ground deformations derived from the InSAR processing of images acquired by the Advanced Synthetic Aperture Radar (ASAR) sensor of ENVISAT from 2002 to 2010. InSAR, combined with GPS, overcomes the limitations of GPS in terms of sparse samplings and weak vertical estimations (except at the permanent stations). It enables accurate (submillimeter) measurement of the vertical velocity at thousands of points, a density not achievable with campaign GPS.

2. Data

We used 29 acquisitions of the ascending track 415 (period 11 February 2003 to 9 February 2010) and 33 of the descending track 279 (period 20 October 2002 to 27 December 2009) acquired by the C-band ASAR

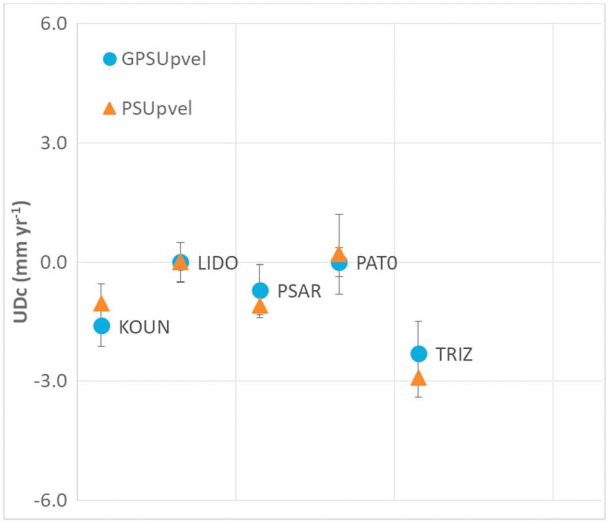

Figure 5. Vertical GPS and InSAR velocity at five permanent GPS stations. EYPA that was affected by the 2010 earthquakes is not available, as is the case with LAMB where the time series is too short.

sensor of ENVISAT in I2 mode with incidence angle ~23°. The digital elevation model used to remove the topographic effect in InSAR was made by the Hellenic cadastre using aerial photogrammetry surveys with pixel size 5 m. Its vertical accuracy is estimated to be ~5 m.

The available GPS velocities are used to anchor to a rigorous geodetic framework the velocities obtained from InSAR. They are from 66 campaign points (Avallone et al., 2004; Briole et al., 2000; Müller et al., 2011) occupied periodically since 1990 and 7 permanent points installed after 2001 (http://crlab.eu). The permanent points have velocities known with accuracy well below 1 mm/year in the three dimensions. At campaign points, horizontal velocities have also 1 mm/year accuracy on average, while the vertical is known within a few millimeter per year only. As all permanent points, except TRIZ which is close to the center of the rift, show no significant vertical velocity, we assume that it is the same, on average, for all campaign points. Using this assumption, the line of sight (LOS) velocities deduced from GPS are used to align, with a least square procedure, the LOS velocities calculated with InSAR. We refer the GPS velocities (and therefore the InSAR velocities) to Peloponnesus accordingly with Avallone et al. (2004).

3. InSAR Processing Along the Ascending and Descending LOSs

Figure S1 shows with lines the interferograms computed for the two tracks. Because of the discontinuity induced by the sea (with possible loss of phase continuity) and because of the ground motions produced by the 18 and 22January 2010 Efpalio earthquakes (Sokos et al., 2012), we produced two sets of interferograms, one tied to the north block, called *North view*, with 115 and 190 ascending and descending interferograms, and one tied to the south block, called *South view*, with 123 and 254 ascending and descending interferograms. The interferograms were made using the TUDelft Doris version 4.02 software (Kampes et al., 2003).

4. Multitemporal Combined PS-SBAS LOS Velocities

There are two main methods of multitemporal InSAR, one called Persistent Scatterers (PS) and the other Small Baseline Subset (SBAS). PS methods are based on the selection of pixels with either stable phase variation in time (e.g., Ferretti et al., 2000, 2001; Kampes, 2005) or high coherence in space (e.g., Hooper et al., 2004; Van der Kooij et al., 2005). SBAS methods (e.g., Berardino et al., 2002; Schmidt & Bürgmann, 2003) combine a limited number of selected interferograms with small orbit separation and therefore small inter-pixels spatial decorrelation due to the stereoscopic effect of the different orbits. PS is more efficient in urban areas while SBAS is more powerful in nonurban areas (Casu et al., 2006). As most of the Corinth rift area is nonurban and mountainous, SBAS provides a significant contribution to the study of the area.

We used the StaMPS/MPI software following the method of Hooper (2008). StaMPS (Stanford Method for PS) is using an algorithm that tracks PS not only in urban areas but also in terrains devoid of man-made structures or undergoing nonsteady deformation. StaMPS/Multitemporal InSAR (Hooper, 2008; Hooper et al., 2004, 2007) is an extension of StaMPS adding SBAS and a multitemporal InSAR method. In this paper, the ground motion is assumed to be steady during the 8 years 2002–2010. The maps shown below combine PS and SBAS (Figures 4 and 5) data sets maximizing the reliability of the unwrapped phase and increasing the signal to noise ratio exploiting the procedure of Hooper (2008). Furthermore, as we will show, we exploited the redundancy of PS and SBAS velocities determined independently for the ascending and descending tracks to validate our results.

For the PS processing of the ascending track the image of 5 August 2003 is used as master. With an amplitude dispersion index of 0.4, 59027 LOS velocities are estimated in the North view and 29171 in the South view. For the

Table 2
RMS Scatter Between InSAR and GPS EW and Vertical Velocities for Two Different Values of the Sampling Radius Around the GPS Points

Component velocity	Radius (km)	RMS scatter (mm/year)	Points used
EW—campaign points	0.4	2.0	44
Vertical—permanent stations	0.4	0.4	6
EW—campaign points	1.0	2.8	66
Vertical—permanent stations	1.0	1.1	7

Note. RMS = root-mean-square.

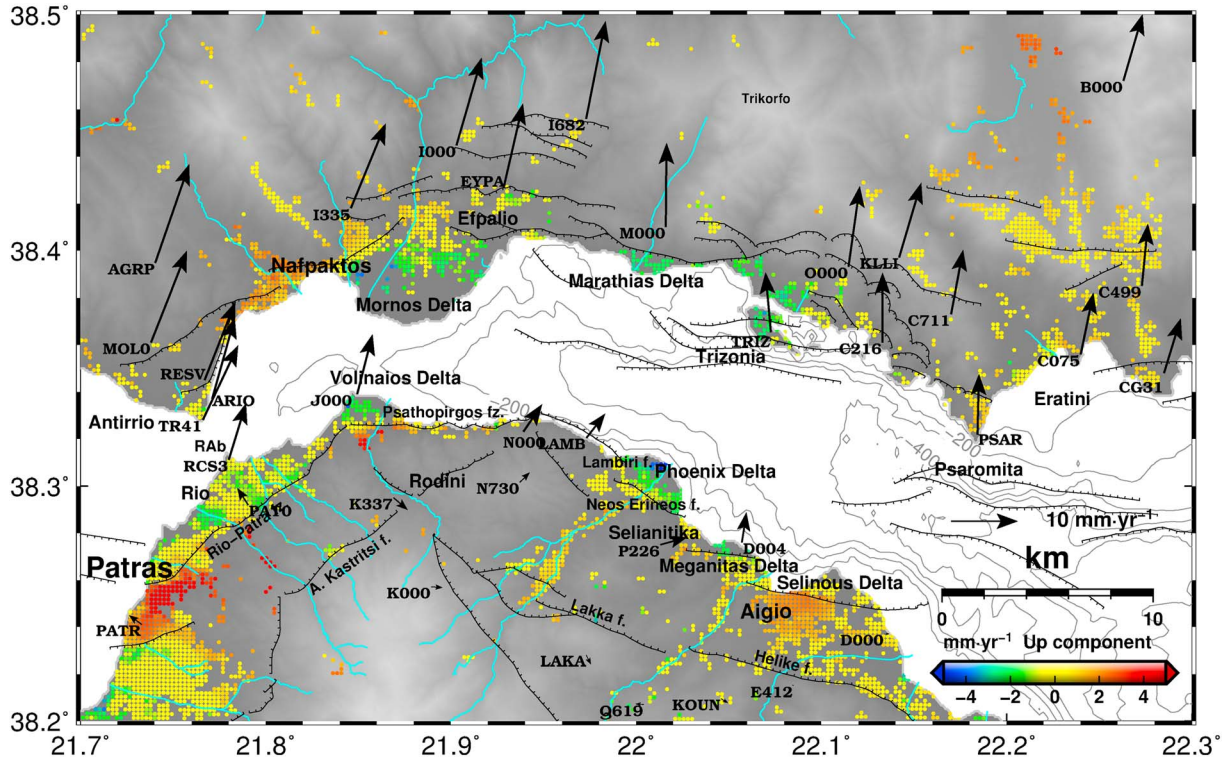

Figure 6. Best constrained 4,391 vertical Persistent Scatterers/Small Baseline Subset velocities for pixels of 200 m. This is the best results when using pixels of 200 × 200 m (doi:10.5281/zenodo.1205496).

SBAS processing, with amplitude dispersion index threshold of 0.6, minimum coherence threshold 0.5, decorrelation threshold 1,700 days and critical baseline 1,070 m, the 115 and 123 interferograms lead to 60331 and 37438 LOS velocities in the North and South views, respectively. The two populations of LOS velocities are almost equally represented but in most cases not at the same location. Their alignment (using the common points) and combination leads to 114553 LOS velocities in the North view and 64322 in the South view.

Similarly, for the descending track the image of 2 November 2008 is used as master in the PS processing which estimates 36489 LOS velocities in the North View and 27580 in the South View. For SBAS, with similar parameters except decorrelation threshold 1,500 days, the 190 and 252 interferograms produce 60683 and 45358 LOS velocities and their alignment and combination with PS 94846 and 71195 LOS velocities in the North and South views, respectively.

In both PS and SBAS methods, the differential atmospheric delay is partly removed assuming that it is spatially correlated up to a distance of a few kilometers. At larger spatial wavelengths, the troposphere cannot be corrected using InSAR internally. This may affect the multitemporal results, but very slightly because of the large population of interferograms participating to the multitemporal analysis. The GPS LOS velocities are used to correct this effect by allowing tilt of the interferograms to compensate possible bias due to systematic lateral tropospheric gradients at wavelength larger than 5–10 km not detectable by InSAR.

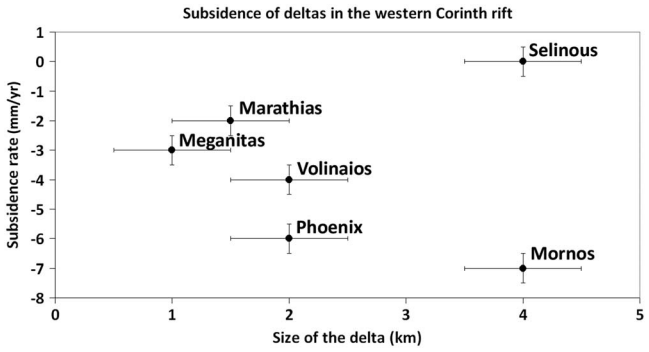

Figure 7. Subsidence rate from InSAR against size of six major river deltas in the western Corinth rift. Size of the delta refers to the length of the river stream along the delta. Subsidence rate refers to the maximum observed rate in the delta at the 25% of points with the highest value (i.e., average the first quartile).

5. Anchoring the InSAR Velocities to the GPS Velocities

At the center of our target area, the incidence vector of the ASAR/ENVISAT in I2 mode, expressed from the ground to the satellite, is ±0.38 (positive for descending), −0.09 and 0.9, respectively in the east, north, and up axis. This vector is variable within the scene in the range −0.406/−0.340,

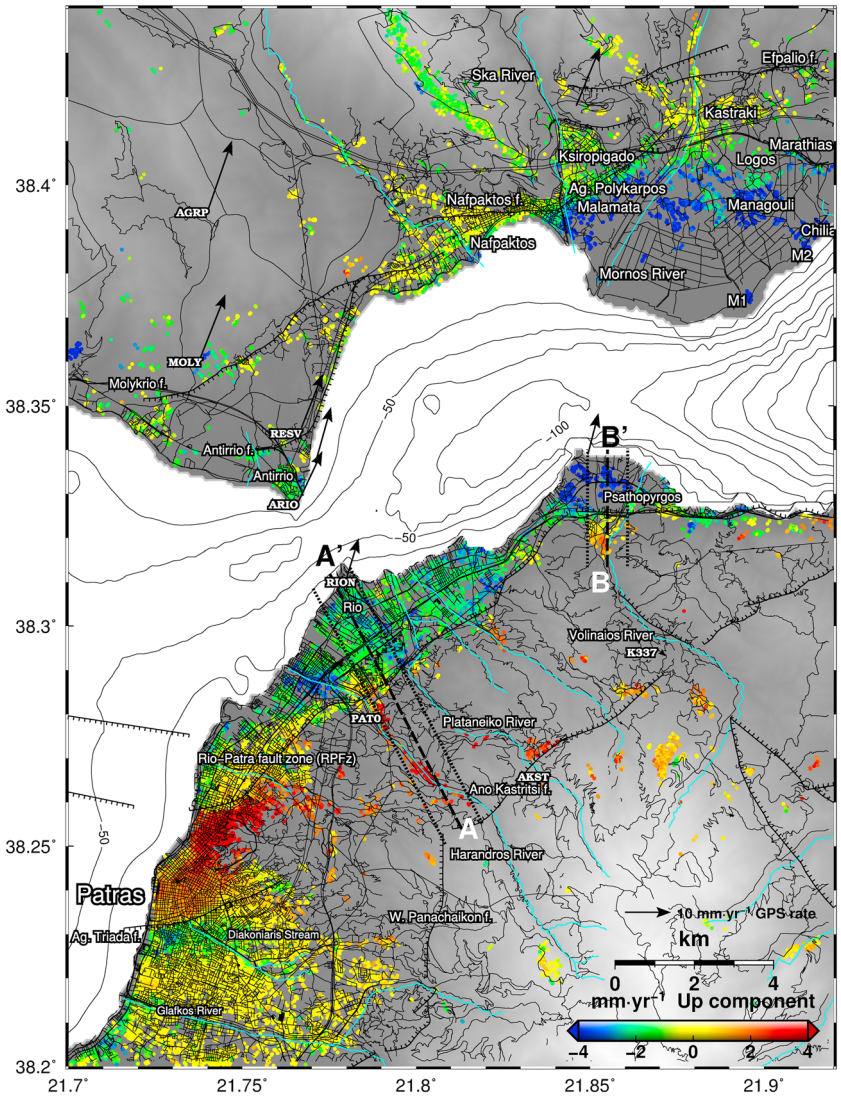

Figure 8. InSAR vertical velocities at the western termination of the Corinth rift, between Nafpaktos and Patras. Solid black lines represent the faults inferred from geological studies, among them the Agia Triada and Rio-Patras faults. The dashed line A-A′ corresponds to section across the Rio-Patras fault shown in Figure 11. The dashed line B-B′ corresponds to the cross sections of Volinaios River Delta in Figure 15. The permanent EUREF GPS point PAT0 (http://www.epncb.oma.be) is shown.

−0.100/−0.084, and 0.937/0.908 in east, north, and up components for ascending tracks and 0.346/0.405, −0.100/−0.086, and 0.909/0.934 for descending.

For both ascending and descending, we estimate, at each GPS points, an average InSAR LOS velocity by using all LOS velocities available within a radius 400 m. The *GPS* LOS velocity is obtained by using the known and accurate horizontal GPS velocity and zero for the vertical velocity except at TRIZ where we use −2 mm/year, and projecting in the LOS. At this stage we have a LOS scatter (between GPS and InSAR), that we call dLOS at the 73 GPS points. Then, by least square minimization, we calculate the best fitting tilt (2 parameters) and offset (1 parameter) to be applied to the 73 dLOS values to minimize them, that is, to have them aligned with the plane Z = 0 in a space with *X*, *Y* the coordinates of the GPS point and *Z* the dLOS.

To assess the improvement of the LOS velocities after dLOS minimization, we calculate the vertical velocities retrieved from InSAR (and using the horizontal GPS values) at the location of the GPS points before and after the correction. For that we assign to the *InSAR* points the horizontal velocity from GPS and estimate the vertical. For the North view, the standard deviation of the velocities (around an imposed average of zero) is 3.6

Table 3
Vertical Velocities in and Around Mornos Delta

Location	Vertical InSAR velocity, current study (mm/year)	Number of PS	Parcharidis et al., 2013 (mm/year)
Nafpaktos	−1.0 ± 1.0	2068	−1
Nafpaktos h/wall	−0.5 ± 0.6	1118	
Managouli	−4.0 ± 0.6	247	−4.5
Chiliadou	−5.0 ± 0.7	58	−4.5
Loggos	−2.0 ± 0.3	47	−2.5
Kastraki	−0.5 ± 0.4	154	−2
Xiropigado	−2.0 ± 0.6	135	−1
Efpalio	−2.0 ± 0.7	334	−2
Malamata	−4.0 ± 0.5	109	−4
Agios Polykarpos	−3.5 ± 0.4	80	−2
Area M1—Nirefs	−7.0 ± 0.7	22	+2 ± 1[a]
Area M2—Nirefs	−9.0 ± 0.7	34	

Note. The values of Parcharidis et al. (2013) are also reported (those values are directly deduced from the line of sight assuming no horizontal relative velocities, and these were shifted by −1 mm/year to be consistent with ours). PS = Persistent Scatterers.
[a]Analysis of the vertical component of the GPS station installed in 2015.

and 1.6 mm/year for ascending tracks and 3.3 and 1.4 mm/year for descending tracks, respectively, before and after correction. For the South view the equivalent numbers are 4.9 and 1.1 mm/year for ascending and 2.4 and 1.6 mm/year for descending. The need and benefit of the alignment on GPS is clearly demonstrated. Figure S2 and Figure S3 show several features that are discussed in detail in the following sections, in particular discontinuities in the city of Patras, Rio, Psathopyrgos, and Selianitika. The vegetated land cover, the steep slopes, and the moisture in the mountains are characterized by strong temporal decorrelation.

6. Determination of the Vertical and East Velocities

This procedure is performed for the north and south views separately. For each pixel of the combined ascending PS-SBAS file, we seek for a companion pixel in the descending combined PS-SBAS fine, by searched within a radius of five pixels (~100 m). This gives us two LOS measurements, and to retrieve a 3-D motion we use as third observation an estimate of the NS velocity derived from bilinear interpolation of the velocities at the 73 points. Despite the large gradients of NS velocity in the Corinth rift, this interpolation is accurate because most of the extension is offshore (see Avallone et al., 2004) with a south block almost rigid and a north block showing smoothly distributed deformation that strongly supports an interpolation. Moreover, as the NS component weights only for ~0.09 in InSAR (NS projection of the incidence vector), the need for accuracy in the NS velocity is not great and the ~1 mm/year accuracy easily achieved in the interpolation between the 73 points is sufficient. The maps of vertical and east-west InSAR velocities are shown in Figure 3 and Figure S4.

7. Comparison of the EW Velocities From GPS and InSAR

In section 5, we used the GPS velocities to anchor the ascending and descending LOS velocities. Here the GPS velocities are used a second time to assess the quality of the 3-D vectors calculated at the selected PS-SBAS pixels in the previous step. This is not a redundant use of the GPS information. Indeed, for the anchoring, we used the long wavelength of the GPS velocity field, while here we use the short wavelength. Only 43 GPS points are used now, that is, the ones located at less than 400 m from the closest PS-SBAS. Our assessment is made by comparing the EW velocities from GPS and from InSAR (Figure 4 and Table 1). The average consistency is not very good with large outliers, and the average scatter is just below 2 mm/year which is more than the theoretical native quality of both techniques. We believe that those outliers are due mainly to unwrapping errors in the InSAR processing at the particular pixel, and in section 8 we will apply a method to mitigate this effect and improve our results.

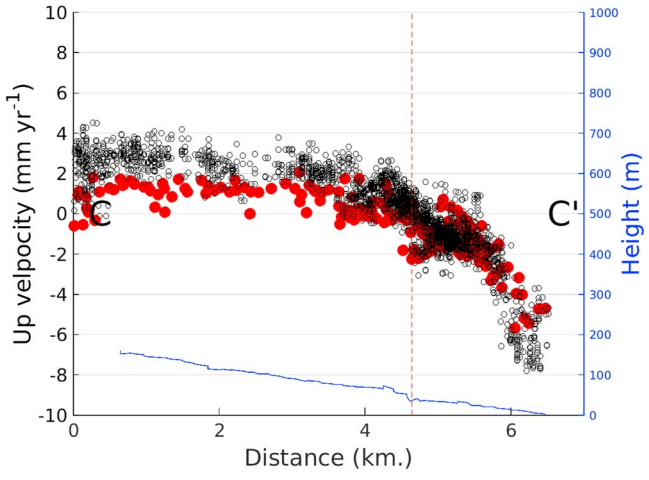

Figure 9. Cross section across the Phoenix River Delta (crossing Selianitika fault) defined as C-C′ in Figure 16. The vertical component of deformation of Persistent Scatterers (circles) and the best constrained 4,391 Persistent Scatterers (red) are shown. The red dashed line indicates the crossing at the fault line shown in Figure 16 as Selianitika f. Blue line corresponds to the altitude along the river projected to the profile (digital elevation model errors and errors in the river location leads to nonmonotonic altitude increasing).

This result, and the quantitative determination of the average scatter, allows a posteriori assessment of the robustness of the anchoring of the InSAR to the GPS velocities, which quality comes from the number of GPS velocities used. Theoretically the combined use of the 73 GPS points allows a drop for the single average scatter of 2 mm/year to an average accuracy of alignment of ~$2/73^{1/2}$, that is, ~0.23 mm/year, thus, using a conservative factor of two, we believe that, after the alignment made in section 5 and based on this comparison, we can estimate that our LOS are detrended globally, at long wavelength, at the level of ±0.5 mm/year. This does not prevent the existence of larger anomalies locally (most probably due to unwrapping errors). The next section is devoted to the identification and removal of those anomalies.

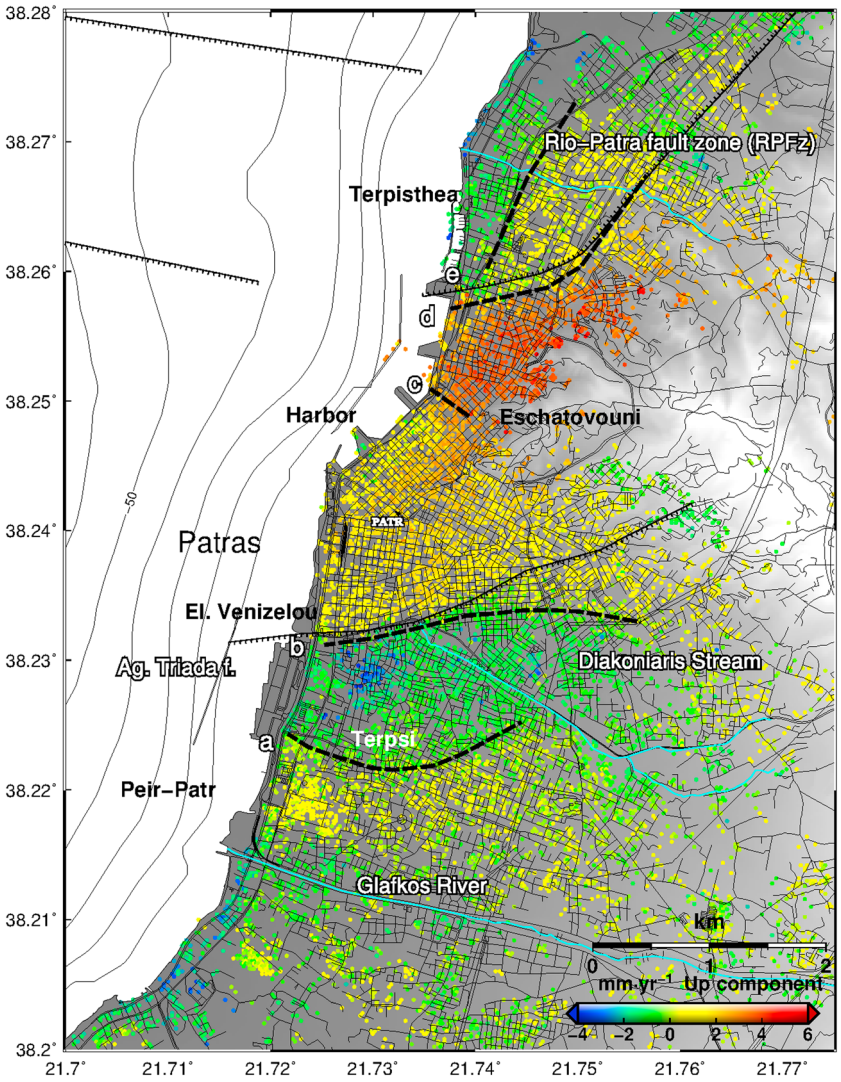

Figure 10. InSAR vertical velocities at the city of Patras. Solid black lines represent the faults inferred from geological studies, among them the Agia Triada and Rio-Patras faults. The dashed lines represent boundaries of structures.

For the vertical, the comparison is possible at the permanent GPS stations only. Figure 5 shows that GPS and InSAR fit within ±0.4 mm/year. Subsidence greater than −2 mm/year for TRIZ (in the Trizonia Island) is consistently quantified with the two methods.

The sensitivity of the solution to the radius of the disk used to select the InSAR pixels was also proven to be averaged around the GPS point. Table 2 shows the difference between our preferred radius of 0.4 km and a radius of 1.0 km. The root-mean-square (RMS) scatter increases with the radius, however the average vertical scatter remains at the level of ±1 mm/year.

As it is expected, the ratio between the RMS in the east and up components (from Table 2) is the same as the 4/9 ratio between those components in the incidence vector. Moreover, the small radius of the disk ensures the same tropospheric conditions among the contributing pixels.

We also analyzed the differences between our determinations for North view and South view at the 32 GPS points which were in both views: the RMS scatter between InSAR and GPS velocities is 1.9 mm/year in east and 0.9 mm/year in up. Again, this is consistent with the scatters found above, and thus enhances the robustness of our accuracy assessment.

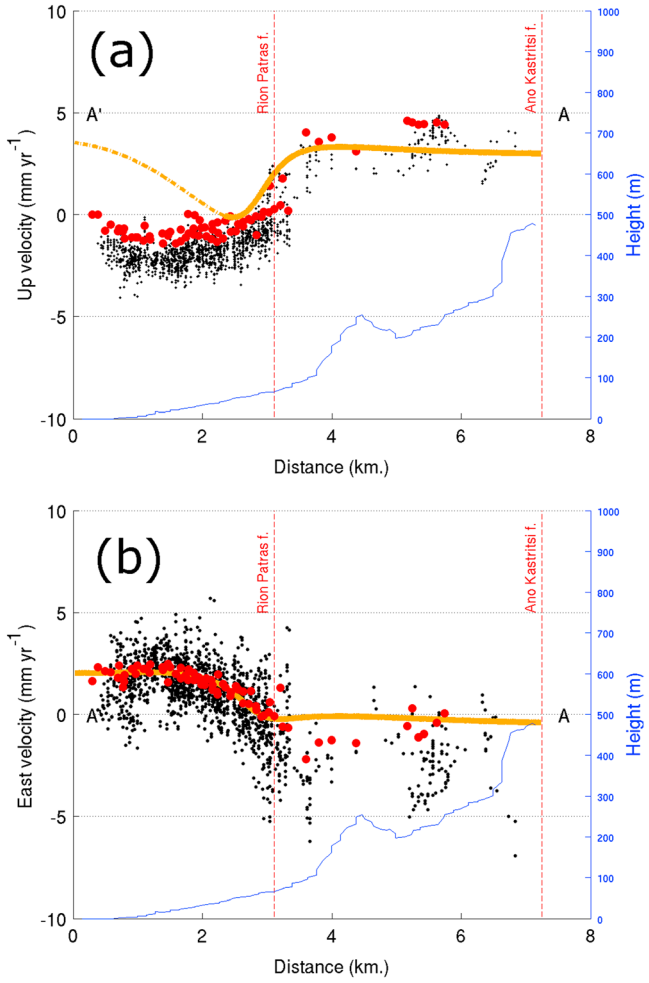

Figure 11. (a) Vertical InSAR velocities across the Rio-Patras fault at the level of the section A-A′ (see Figure 8). The blue line is the elevation profile along the section. The selected pixels are those located between the two dotted lines visible on both sides of the section in Figure 8. The red dots are the best constrained 4391 data set, the black points are the original velocities using all selected pixels. The orange line is the prediction of the model. (b) Same as (a) but for the eastward velocities (with respect to Peloponnesus).

8. Improved Vertical and East-West Velocities by Using Larger Pixels

In this last processing step, the accuracy is improved by considering larger pixels of 200 m, and by combining north and south views and by reanalyzing separately the original PS and SBAS velocities. First, the LOS velocities are resampled at 200 m. The loss in spatial resolution results in a gain in the accuracy of the velocities. It leads also to a loss of information in the low coherence areas. Indeed, we keep only the large pixels that contain at least two small pixels from the original set. Moreover, each of those small pixels must have its full set of measurements, that is, two PS ascending velocities, one in the North view and one in the South view, two SBAS ascending velocities, one per view and the same four PS and SBAS measurements for the descending view. Finally, for each remaining large pixel, we discard the pixel if at least one of the scatters between the four ascending or descending velocities is larger than 1.5 mm/year.

The wealth of information provided by the availability of eight measurements per original pixel and the combination of several original pixels allows tracking efficiently the unwrapping errors not eliminated in the previous steps. At the grid points having passed successfully this screening (Figure 6), the average RMS scatters are 0.45 and 0.44 mm/year for the vertical and east-west velocities. This procedure formed the set *S1* of best constrained 4,391 points (Table S1). We produced also a file with 951 points only (Table S2) by lowering from 1.5 to 1.0 mm/year the selection criteria indicated in the previous paragraph. We estimate the average accuracy of this set *S2* to be ~0.5 mm/year, it is the one that we recommend for further use. Its weakness is the lack of information in some areas with moderate or low coherence, but 951 points with velocities known at this level of accuracy means more than 10 times more InSAR velocities than GPS velocities with equivalent quality, thus a great (and geodetically controlled by the GPS) densification of the mapping of the ground deformation in the area.

The vertical velocities that are analyzed and modeled in the next sections are those of initial vertical and east west PS/SBAS velocities as in Figure 3 (with less accurate but more pixels), S1 set as in Figure 6 (with less pixels and more accurate), and S2 set (with few pixels and the highest accuracy). These different determinations show consistency in several deforming areas along both sides of the rift. Along the South coast, moving from west to east, we see various deforming zones inside Patras with uplift and subsidence, subsidence in Rio, uplift and subsidence near Psathopyrgos, subsidence in Selianitika, uplift in Aigion. Along the north coast, moving from west to east, we see moderate uplift in the city of Nafpaktos and subsidence in the Mornos and Marathias deltas.

In the following, we focus upon areas of special interest. Color scales may be different with respect to the previous sections in order to enhance the vision of the ground deformation. We discuss first the question

Table 4
Parameters of the Model for the Rio-Patras Fault at the Latitude of Rio and the Rio-Antirio bridge

Unit	X upper center UTM (km)	Y upper center UTM (km)	Azimuth (°)	Length (km)	Width (km)	Depth of upper edge (km)	Rake (°)	Dip (°)	Slip (mm/year)
F1	570 ± 1	4,239 ± 1	233 ± 5	9 ± 1	2 ± .5	0.6 ± 0.3	−120 ± 10	45 ± 10	8.7 ± 1
F2	556 ± 1	4219 ± 1	30 ± 5	20	15	2 ± 0.5	−90 ± 10	90[a]	15 ± 1

[a]F2 is assumed to be vertical and its dip angle was not inverted

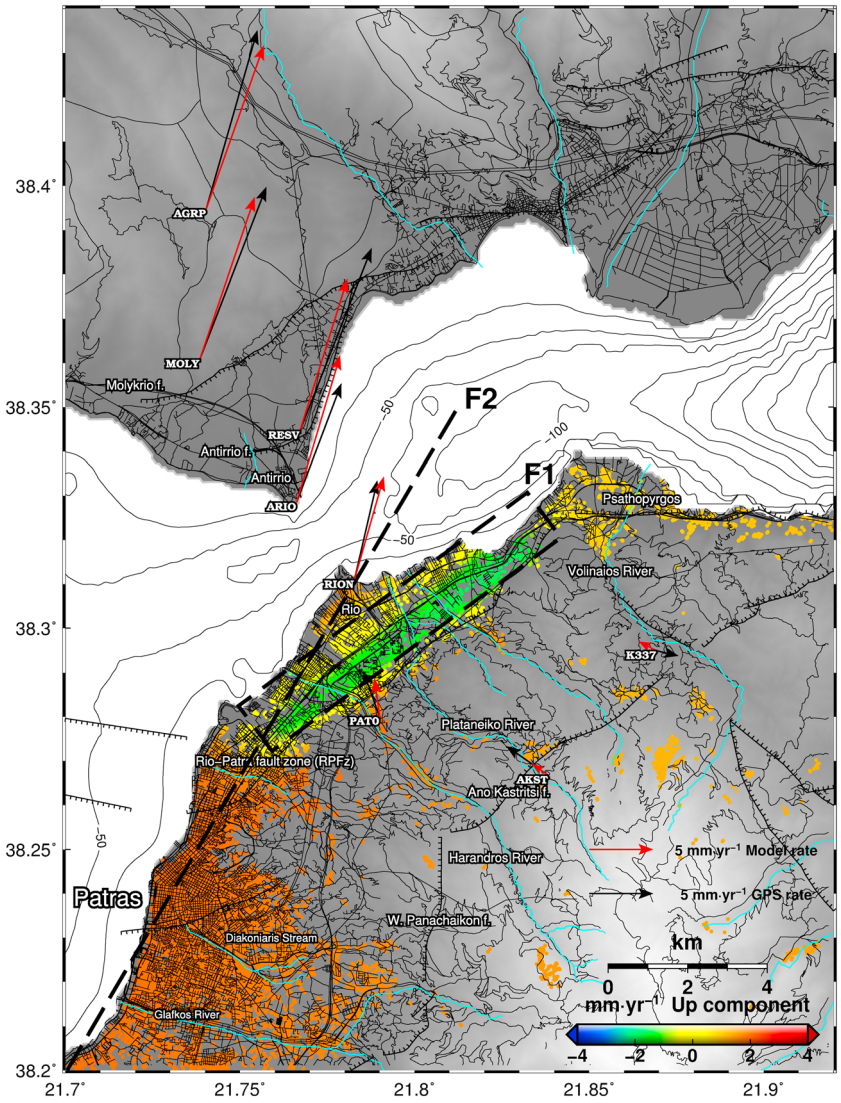

Figure 12. Model of ground deformation induced by a hypothetical Rio-Patras fault marked by the dashed black rectangle F1 and line F2. F1 is a shallow transtensional normal fault and F2 is a vertical right lateral strike slip fault. The faults parameters are in Table 4. Observed and modeled GPS velocities (Table 5) are marked with black and red arrows. With a horizontal velocity which is right at the middle of the gradient, the area of the Rio Castle lies right above the inferred strike slip fault.

Table 5
Fit of the GPS Velocities (Observed and Calculated)

Code	Latitude(°)	Longitude (°)	East vel. GNSS (mm/year)	North vel. GNSS (mm/year)	East vel. Model (mm/year)	North vel. Model (mm/year)	X UTM (km)	Y UTM (km)
AGRP	21.74031	38.39472	4.0	14.0	4.5	12.8	564.65	4,249.87
MOLY	21.73845	38.36078	5.4	13.5	4.3	12.7	564.52	4,246.10
RESV	21.76718	38.34464	5.6	14.3	3.7	11.9	567.04	4,244.33
ARIO	21.76621	38.32849	3.5	9.3	3.4	11.5	566.97	4,242.54
RION	21.78273	38.31090	1.8	7.8	2.3	8.1	568.43	4,240.60
PAT0	21.79000	38.28000	−1.3	3.6	−0.4	3.0	569.10	4,237.18
AKST	21.83835	38.26669	−3.3	2.3	−1.3	0.9	573.34	4,235.74
K337	21.86937	38.29494	1.7	−0.4	−1.4	0.7	576.02	4,238.90

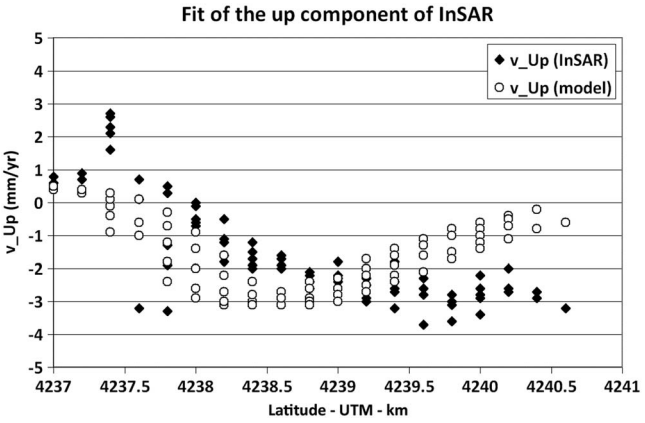

Figure 13. Fit of our model for the vertical component of InSAR (for 76 points of the *S2* set located along a RION-PAT0 profile of 3 km length).

of the river deltas, then the question of the urban subsidence. Those two aspects of the ground deformation, often visible in InSAR, and this is the case here, alter the message of tectonic origin and need to be corrected before any tectonic analysis and modeling. Finally, and base on this prerequisite, we analyze and model the relatively large and localized deformations that we observe in the Rio-Patras area, north of Patras, and in Aigion where the large earthquake of 15 June 1995 occurred and where InSAR suggests the existence of a postseismic signal during the ENVISAT era 2002–2010.

9. The Deltas

There are several deltas in the Corinth rift showing a clear deformation signal and there is also the Selinous delta, one of the largest, showing no deformation. Figure 7 summarizes the observed characteristics of six of those deltas.

9.1. The Mornos Delta

Figure 8 shows the subsidence in the Mornos delta. This subsidence was already described by Parcharidis et al. (2013). Its main cause is presumably the compaction of sediments by consolidation of the dewatered material and the load of the subsequent overlain deposits (Parcharidis et al., 2013). However, there might be other causes of vertical movements in the deltas, especially the large ones and those with agriculture, in response to changes of the underlying water table in relation with the exploitation of the aquifer or climatic fluctuations.

In two small areas of the Mornos delta near the SSE coast of the delta (locations M1 and M2), there are buildings of fish farms producing coherent pixels with InSAR subsidence rates of 7 and 9 mm/year. Table 3 gives values at other spots and a comparison with the LOS rates of Parcharidis et al. (2013). Those high subsidence rates might not be steady. Indeed, the analysis of the vertical coordinate of the permanent GPS station XILI installed at M1 location indicates uplift for the recent period 2015–2017 at a rate of 2 mm/year. If confirmed, this will strengthen the need of refined analysis of the role of the aquifers in the subsidence of this and other deltas in the area.

9.2. The Phoenix Delta

This river delta is relatively small in size but drains one of the major rivers of the area and it is, with Mornos, the delta with the largest subsidence rate during the analyzed period. Along the profile C-C′ (depicted in Figure 16), the gradient of subsidence (Figure 9) is high when entering the delta.

10. Ground Deformation in Downtown Patras

In Figure 10, moving from Glafkos river to the south toward the Rio-Patras fault zone in the north, we can discriminate five domains each one bound by the features “a,” “b,” “c,” and “e.” The Terpsi area, between the sharp discontinuities a and b, corresponds to the ancient valley of the Diakoniaris stream. The area located between c and d correspond to the extremity of the oblique part of the Rio-Patras fault, with the fault becoming purely strike slip further south. This area undergoes fast uplift in the analyzed period, which we interpret as a tectonic effect related to the change of azimuth of the fault. In our model, d is the actual beginning of the shallow Rio-Patras fault (see also Figure 8). Other local urban deformations can be observed, with subsidence south of Terpi, an uplift in Peiraiki-Patraiki, in Terpsithea and south-west of Eschatovouni.

Parcharidis et al. (2009) studied the ground deformation in Patras using 42 ERS1 and ERS2 SAR scenes acquired between 1992 and 2000 along the descending track 279, with the Image Processing Theory, Tools and

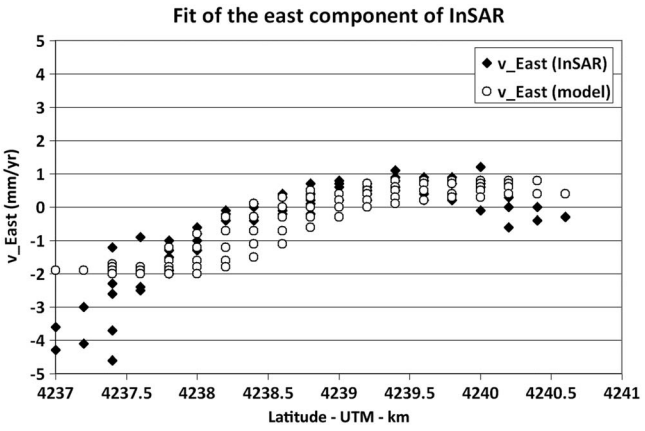

Figure 14. Fit of our model for the E-W component of InSAR (for 76 points of the *S2* set located along a RION-PAT0 profile of 3 km length).

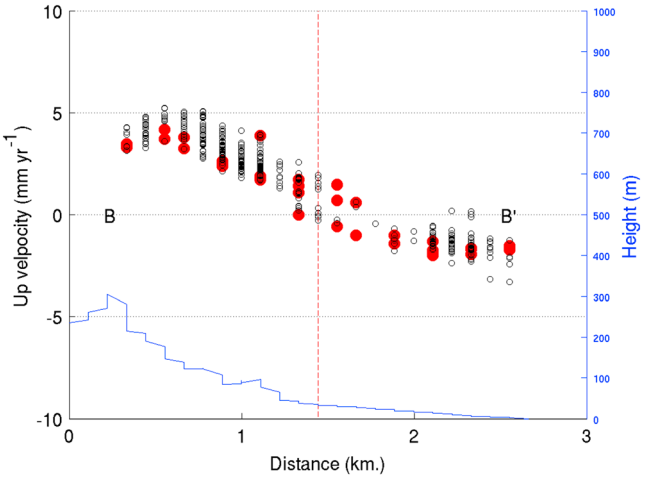

Figure 15. Vertical InSAR velocities across the Psathopyrgos fault (marked by the red dotted line) at the level of the section B-B′ (see Figure 8) located in Volinaios river delta. Red dots are from the best constrained 4,391 data set using large (200 m) pixels. Black points are the original velocities using all selected pixels. The blue line is the elevation of the river bed projected to the profile (errors in the river location and digital elevation model errors lead to nonmonotonic altitude in function of distance).

Applications processing scheme. The discontinuities they describe agree with those presented here, thus they appear to be persistent for ~20 years (1992–2010). Based on fieldwork and aerial photo interpretation, Koukis et al. (2005) proposed the existence of other shallow faults in Patras, that could be related to some of the features visible in Figure 10, that is, a, b, along harbor, striking SW, c, d, and e. On 31 August 1989 a shallow earthquake of M_S = 4.8 occurred in Patras. Kalteziotis et al. (1991) reported unusual large ground deformation for such a magnitude along the discontinuity b. They proposed, as well as Koukis et al. (2005), the existence of a shallow normal south dipping structure that they called the Agia Triada fault, and Athanasopoulos and Leonidou (1996) modeled the observed displacements assuming the coseismic deformation of a fault of 1,200 m length and 388 m width which is reaching the surface. However, those papers do not bring proofs that the motion across this Agia Triada structure is directly related to the coseismic fault plane. There is no clear evidence of the existence of such an active tectonic fault at shallow depths. The 1989 displacements might be the result of a gravitational slip along the northern bank of the ancient Diakoniaris river. In the last decades, this river had been progressively channelized and covered by the urban sprawl. The graben, still visible today in the city and in the subsidence (between a and b), is most probably due to residual compaction of the area.

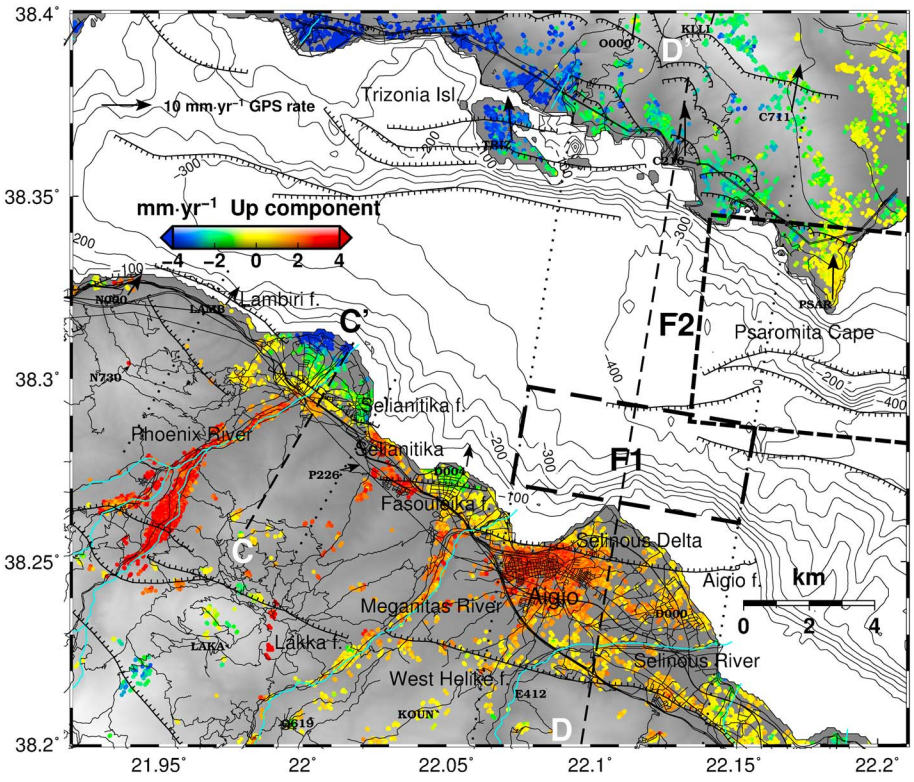

Figure 16. Vertical InSAR velocities in the area of Aigion, Lambiri, Trizonia, and Psaromita. The black dashed line C-C′ corresponds to the cross sections of Phoenix River Delta (crossing Selianitika fault) plotted in Figure 9. The black dashed line D-D′ corresponds to the cross sections of Aigion (crossing the Aigion fault) plotted in Figure 21. The black dotted lines correspond to the extension of the sampling for the profiles. F1 represents the modeled aseismic fault active during the analyzed period. F2 represents the coseismic fault that occurred in 1995 as calculated by Bernard et al. (1997).

Table 6
The Aigion Fault Parameters From Various Studies

Reference	Slip rate	Surface vertical rate	Length	Width	Dip angle	Upper depth
Unit	mm/year	mm/year	km	km	°	km
Moretti et al. (2003)		2–5			55–70	Fault exposed at the surface
De Martini et al. (2004)	9–11	1.05–1.2	10	9.5	50	0.2
Moretti et al. (2004)		3.5				
Pantosti et al. (2004)	1.6–6.3	1–4.1	8–14		60	Fault exposed at the surface
Lykousis et al. (2007)		3.4			60	
Bernard et al. (2006)			10 ± 1	10 ± 2	60	0
McNeill et al. (2007)[a]	2.5–4.5		~10		60	
Console et al. (2013)	6		16	10		

[a]In that paper, Aigion to offshore Aigion fault system are considered as one single structure.

11. The Rio-Patras Fault and the Junction With the Psathopyrgos Fault

In Figure 8 abrupt deformation features are visible in the cities of Patras and Rio. Several of these are aligned approximately WNW-ESE. In the north, near Rio, the location of the discontinuity fits well with the location of the known Rio-Patras fault.

11.1. The Rio-Patras Fault

With a NNE-SSW azimuth, the Rio-Patras fault runs inland north of Patras, beneath the city of Rio, where it is visible in the topography and has been previously analyzed using InSAR by Parcharidis et al. (2009). Further south it runs offshore in front of downtown Patras and is presumed to continue along the coastline to connect more to the south with the fault of the 2008 Movri earthquake (Serpetsidaki et al., 2014). The fault, that extends west of the Panachaikon Mountain with a narrow coastal plain hosting large alluvial fans (Flotte et al., 2005; Stamatopoulos et al., 2004), is transtensional with a combination of normal and right lateral slips. The rate of vertical deformation across the fault is clearly visible in the InSAR velocities map (Figure 8) along the valley of the Harandros river (profile A-A′). This valley is the only place where a good continuous profile (Figure 11a) can be extracted from the InSAR velocity map, thanks to the exposure of bedrock along the river bed and the peri-urban land cover. In all other mountain front locations, the land is composed of bush and cultivated slopes with significant erosion often enhanced locally by fires, and therefore has, as a consequence, a low number of available pixels in our velocity map (and many of these disappear in the velocity map of large pixels).

There is a high step in velocity, ~5 mm/year, between the Rio coastline and the mountain. Part of this step may be due to land subsidence in the urban area of Rio (as well as due to the recent sedimentary material) along the coastline, but from the spatial analysis of the data we infer that this effect cannot be large, thus most of the vertical velocity gradient should be produced by tectonic activity. The eastward velocity gradient along the profile A-A′ (Figure 11b) gives strong constraint on the strike slip component of the fault kinematics. With amplitude of ~5 mm/year, the eastward offset is equal to the vertical one and, being horizontal, cannot be biased by anthropogenic causes. It is therefore a robust observation for the quantification and modeling of the activity of the fault.

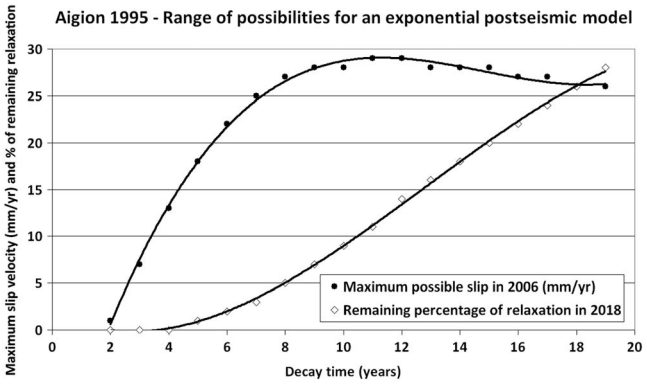

Figure 17. Range of possible slip and percentage of the deformation not yet relaxed in 2018 as a function of the relaxation time.

To model the GPS and InSAR velocities, we assume a fault system locked in part of the crust and slowly slipping elsewhere. For our model we make two basic assumptions: (a) the observed ground motion is due to slip of a planar and rectangular fault (or shear of a volume that can be assimilated to a fault from the observation points) and (b) the medium is a homogeneous elastic half-space. For modeling we use the program developed by Briole et al. (1986) based on the formalism of Okada (1992) and the inversion algorithm of Tarantola and Valette (1982), see Briole (2017) for the

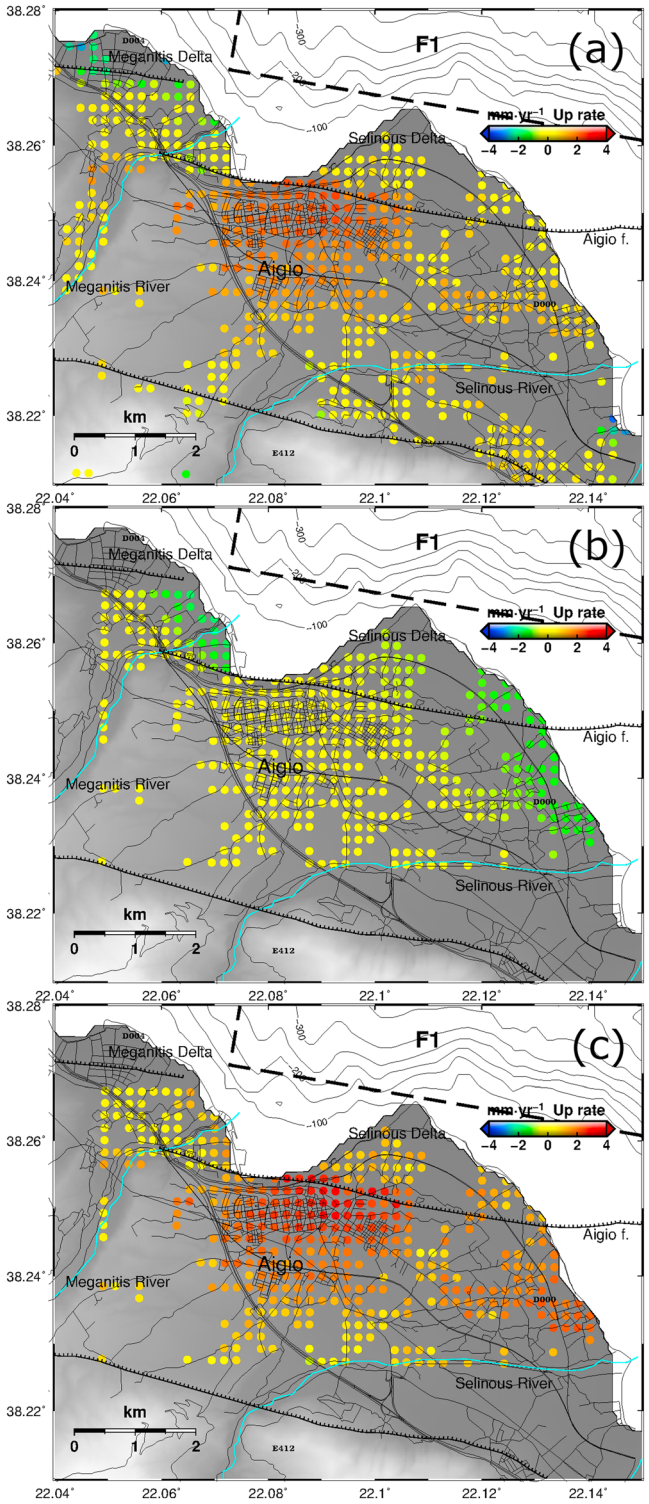

Figure 18. (a) Vertical velocities from the S1 data set over the Aigion area, (b) modeled deltaic subsidence, (c) vertical velocities after correction of the deltaic subsidence.

computer code. The elastic hypothesis is a weak approximation for faults at shallow depth and we know that, in our case, this assumption may lead to underestimating the source depth by typically 0.5 km (Cattin et al., 1999). In the absence of a recent large earthquake, the current ground deformation should correspond to the strain accumulation in the locked areas.

We model the data with two fault segments: a vertical purely strike slip fault (F2) aligned with the coastline of Patras and the azimuth of the Movri 2008 fault zone and a shallow transtensional fault (F1) with azimuth intermediately between the Rio-Patra and the Psathopyrgos faults azimuths. Table 4 gives the parameters of the model and in Figure 12 the model in the location of the PS points as well as the observed and modeled GPS velocities are plotted. The RMS fit of the vertical InSAR velocities and the model is 1.3 mm/year. The RMS fit of the horizontal GPS data and the model is 2.5 and 2.0 mm/year for the north and the south component, respectively. Table 5 lists location and observed and modeled horizontal velocities at the eight GPS points used as input in the model. Figures 13 and 14 show the fit for the vertical and east-west component of InSAR for a subset of 76 grid points of best constrained 951 points (S2 data set) located in the segment of the profile A-A′ (3 km long and 1 km with northern edge at the GNSS point RION and southern at point PAT0, as in Figure 8 and Table 5). In the profile of Figure 13 from the latitude 4240 and to the north, subsidence of the Rio area (due to sediment compaction or underground water drainage processes, parallel to the profile line) close to the coast (i.e., in the hanging wall of the fault between the shore and the fault line) could explain the difference between model and observation. Like in Figure 11 the fit is quite good for the EW InSAR with RMS scatter between observations and model of 0.6 mm/year (i.e., at the level of the accuracy of our data). It is less good for the vertical with an RMS scatter of 1.3 mm/year but the trend for the modeled vertical is quite consistent with the trend of the observed InSAR vertical.

11.2. The Psathopyrgos Fault

In the area of the Psathopyrgos fault the vertical InSAR velocities show an offset of ~5 mm/year across the fault with an extension of the gradient zone of ~2 km (Figure 15), thus wider than the one observed for Rio-Patras. The improved and initial curves of velocities have the same shape but they are shifted by 2.5 mm/year in average, one with respect to the other, the improved one indicating much less subsidence in the hanging wall side.

12. The Aigion Fault

Figure 16 shows the subsidence in the Meganitis and Phoenix deltas. It shows also that the large Selinous delta is not subsiding (see also Figure 7). We believe that this is due to the fact that the subsidence is balanced there by tectonic uplift produced by the offshore part of the Aigion fault, east of Aigion and/or other offshore active structure. There is a clear uplift of the downtown Aigion that is located on top of the eponym fault, and was heavily damaged by the 15 June 1995 M_w = 6.2 earthquake. According to Bernard et al. (1997), the fault where the earthquake occurred is located offshore north-east of Aigion.

The Aigion fault belongs to the set of large north-dipping active normal faults (Bernard et al., 2006) that bound the southern side of the Gulf of Corinth. It has a clear geomorphic expression at the surface in its

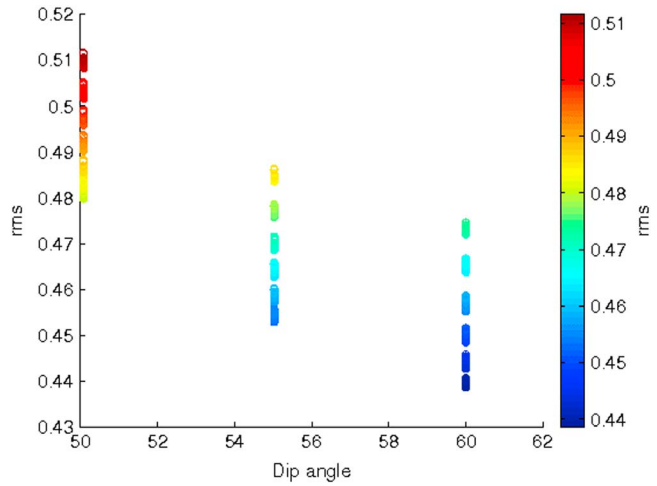

Figure 19. Best fit of the vertical data from S1 set, as a function of the assumed dip angle. RMS = root-mean-square.

middle part (Bernard et al., 2006; Moretti et al., 2003; Pantosti et al., 2004), where it forms a steep escarpment of ~150 m height. De Martini et al. (2004) obtained long-term cumulative uplift rates over the past 200–300 kyr (using U series dating) for the Aigion fault footwall terraces near the edge which were 1.2 and 1.05 mm/year further, which is smaller than the present study and in concordance with Moretti et al. (2003, 2004), Pantosti et al. (2004), and Lykousis et al. (2007). To the east, sonar surveys (Soter & Katsonopoulou, 1999) indicate a likely 3-km long extension of the fault offshore. Where the fault enters the young deposits of the Selinous River delta, the deformation signal vanishes, which we interpret as a consequence of the vicinity of the fault termination and/or the dominant effect of alluvial processes with respect to tectonics.

West of the Meganitis River, the fault geomorphology of the Aigion fault becomes subtle with a main structure paralleled by other minor faults forming a complex step over. Scarps on young delta sediments along the Fasouleika and Selianitika faults (located to the NW) may represent splays of the westernmost portion of the Aigion Fault (Pantosti et al., 2004). Table 6 lists the Aigion fault parameters proposed by different authors.

Bernard et al. (2006) and Lambotte et al. (2014) propose that the Aigion fault roots into the seismically active layer at ~6 km depth with continuous slip on the detachment zone. At intermediate depths it may be subject to seismic slow slipping and they consider that it is locked at shallow depths above ~4 km. In one instance, data acquired at a borehole drilled in 2002 through the Aigion fault (Doan & Cornet, 2007) showed a small deformation signal at the time that seismic waves associated with a large remote earthquake where passing through the area. This transient signal was interpreted as a small slip on the Aigion fault triggered by those long period waves. Also based on the analysis of borehole data and models of pore pressure diffusion, Cornet and Bourouis (2013) proposed that the Aigion fault is slow slipping down to a depth of 5 km or more. Duverger et al. (2015) analyzed the seismic multiplets activated around 7 km depth during the 2003–2004 seismic swarm in the western Corinth rift that were modeled assuming a hydromechanical process. They suggest aseismic slow slipping in the Aigion fault. The Selinous river delta does not seem to subside as all the other deltas do, since we cannot see any deformation gradient toward the coast.

The InSAR velocity map (Figure 16) shows that the city of Aigion undergoes localized uplift of 2–3 mm/year during the sampled period 2002–2010. This area is very close to the fault of the 1995 earthquake (see Bernard et al., 1997) and therefore it may correspond to a transient postseismic movement. Indeed, over long periods of time, we do not expect such high uplift rate at Aigion. The Aigion fault is known to be recent (a few hundred thousand years) and active, the geologically recent relative motion on it may be, possibly, as large as 4 mm/year (i.e., ~3 mm/year subsidence of the hanging wall and 1 mm/year uplift of the footwall), so as to fit with the size of the fault scarp, but not two or three times this value. Therefore, we believe that what we observe at Aigion with ENVISAT from 2002 to 2010 is a transient phenomenon. Below we investigate the hypothesis of a postseismic deformation following the M_w = 6 15 June 1995 Aigion earthquake.

12.1. Assumptions for the Modeling as a Postseismic Process

For our modeling we make simple hypothesis, possibly too simple to explain in-depth the phenomenon, but sufficient to derive some robust information related to the process, in particular its location, its depth, its

Table 7
Parameters of the Slow Slipping Fault for the Postseismic Period 1992–2000 at Aigion (First Line) and Parameters of the M = 6.2 Earthquake of June 1995 (Second Line)

Parameter	E top center UTM	N top center UTM	Azimuth	Length	Width	Depth of top	Rake	Dip	Slip
Unit	km	km	°	km	km	km	°	°	mm/year
Postseismic	597.3 ± 0.7	4235.9 ± 0.7	279 ± 2	7 ± 1.0	6 ± 1.5	1.1 ± 0.2	−90	60 ± 5	22 ± 3
15 June 1995			275	15	9	2.5	−83	35	870

Note. The slip in the model represents the average for the period (i.e., centered in 2006) and it follows an exponential law with decay time of 6 years. We also list in the table the parameters of the 1995 earthquake according to Bernard et al. (1997).

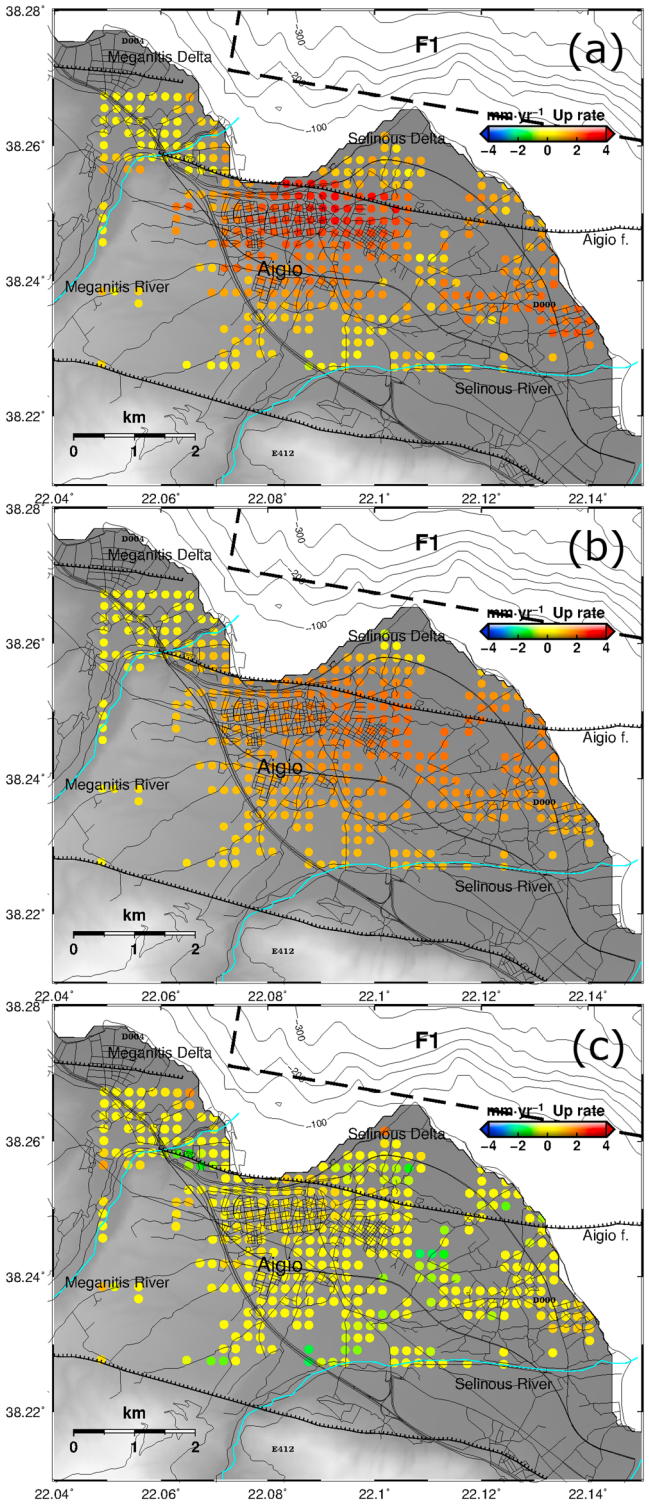

Figure 20. (a) Vertical velocities of best constrained data set 4,391 (*S1*) corrected from the deltaic subsidence (see Figure 18), (b) modeled ground motion assuming the fault of Table 7, (c) residuals.

amplitude, its duration, and therefore help for further refined modeling and interpretations. The first assumption is that the observed motion can be represented by the slow slipping on a fault in an elastic half-space, thus the same process as for the coseismic. We know also that, as our data are not in the immediate near field of the fault tips, a shear in a relatively flat volume (of say 2 km thickness) would be undistinguishable from a purely planar dislocation, thus we do not necessarily need to invoke after-slip on a fault, but any process that might mimic after-slip because occurring in a similar volume in the medium. Second, we assume that the process can be modeled with a simple exponential relaxation low, thus proportional to $e^{-t/T}$ where T is the relaxation time of the process. Third, we assume that the final cumulated postseismic slip cannot exceed the 0.87 m inferred for the coseismic slip during the 1995 earthquake (Bernard et al., 1997). Under those hypothesis we can calculate, as a function of the variable T, the maximum achievable slip in 2006 (the mean epoch of our InSAR results) is thus 9 years after the earthquake. Figure 17 presents the range of possible slip and percentage of the deformation not yet relaxed in 2010 as a function of T. It shows that the maximum value for the slip is 29 mm/year. Any larger value would contradict our third assumption. Figure 17 shows also that for $T \geq 7$ the maximum possible slip is almost independent from T. We know also from our GPS observations (e.g., Avallone et al., 2004) that, apart the coseismic signal associated with the 1995 earthquake, no temporal changes are visible in the GPS time series of campaign points, including those located in the near field of the 1995 and Aigion, in particular the points D000 and D004 (coordinates in Table 1). This discards a too short relaxation time with large amplitude, because such phenomenon would have signed the time series of D000 and D004 which is not the case. Finally the large amplitude of the observed signal (2–3 mm/year) is not compatible with small values of the slip rate in depth (referred from now on as slip). Performing a first series of tests, we found that the most plausible range for T and the slip for fitting our data are 5–7 years and 18–26 mm/year, and in the following we assume T = 6 years and a slip in 2006 of 22 mm/year, which means according with the exponential law, ranging from 43 mm/year in 2002 to 11 mm/year in 2010. In this scenario Figure 17 shows also that the process is almost terminated today with only 4% of relaxation remaining, which means that, if our model is correct, the uplift signal should not exist in the interferometric data of the ESA SENTINEL-1 acquisitions which started on October 2014.

12.2. Separating Delta Subsidence and Tectonic Movement

Before modeling the ground deformation, we must separate the tectonic signal from the subsidence in the deltas that are located east and west of the uplifted area. For the Meganitis delta we consider a linear increase of subsidence toward the coast close to the current riverbed of 2 mm·year^{-1}·km^{-1}, a value inferred from Ford et al. (2007) who also give a maximum subsidence of 2 mm/year in the Vouraikos delta, which has a size comparable to the Meganitis one. For the Selinous delta we use the mean value of subsidence given by McNeill et al. (2007), (estimated as ~1.3–2.5 mm/year), of 2 mm/year as the maximum subsidence of the coast located close to the current riverbed and decreasing to half toward the Northern cape (along the coast). This rate agrees with that of the Vouraikos delta, of 2 mm in ~1 km width. The subsidence is decreasing moving away the coast. Figure 18 shows the original data from the S1 set, the subsidence signal estimated with

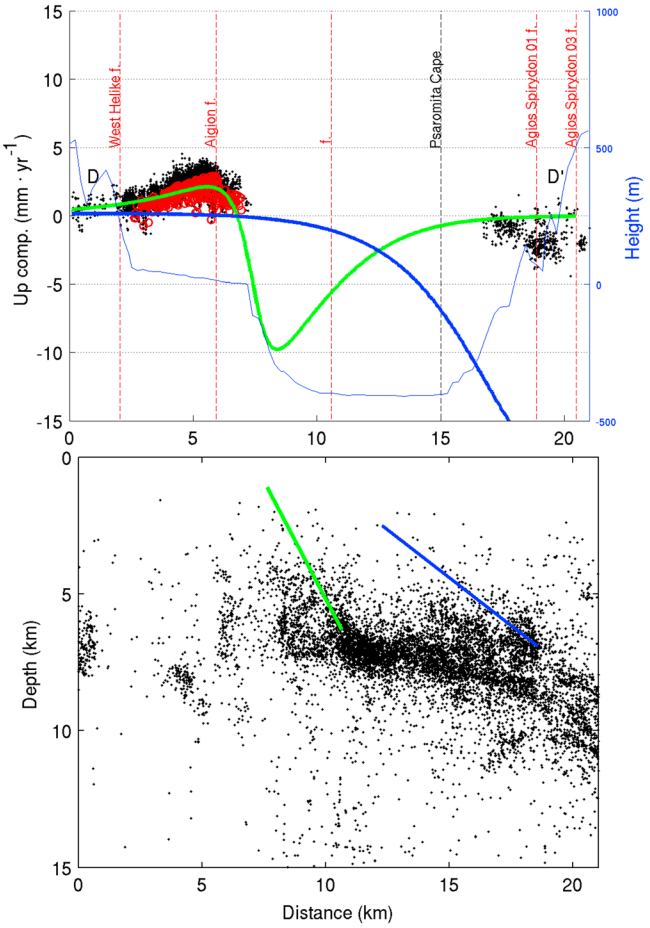

Figure 21. Cross section across Aigion (crossing Aigion fault) defined as D-D′ in Figure 16. Up: The vertical component of deformation rates of Persistent Scatterers (circles) and the best constrained 4,391 data set (red) are shown. The green solid line indicates the vertical modeled component of the deformation rate of slow slipping fault. The blue line indicates the vertical modeled component of the deformation of the 1995 Aigion earthquake (Bernard et al., 1997). The red dashed lines indicate crossing of the fault lines shown in Figure 16. Blue line corresponds to the altitude. Down: Relocated seismicity from 2000 to 2007 (Lambotte et al., 2014), data at http://catalogs.crlab.eu. The red solid line indicates the fault trace of the modeled slow slipping fault and the blue one the modeled 1995 Aigion earthquake (Bernard et al., 1997) fault trace.

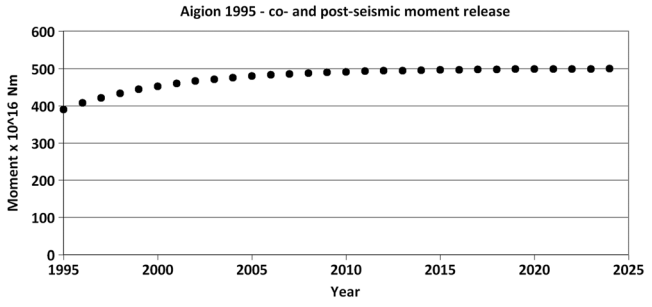

Figure 22. Temporal evolution of the seismic moment release in our best-fitting model.

the above hypothesis, and the data corrected for the subsidence in the deltas, thus the data that will be used for inferring the parameters of the assumed fault (or fault zone).

12.3. Parameters of the Best Fitting Postseismic Model

Although our data are, in principle, corrected for the deltaic subsidence, we exclude for the inversion the points located around the Fasouleika fault (Figure 16) in Meganitis river delta, so as not to be contaminated by possible outliers there.

We explore the space of solutions by performing series of inversion and analysis of the fits and parameters correlations. In all trials we assume pure normal mechanism. Our first series of inversions indicate that the fault is relatively shallow with tip at ~1 km depth and bottom at ~7 km depth. At such depth the fault is expect to be relatively steep, possibly between the 60° and 65° of the uppermost part of the Aigion fault as constraint by the studies related to the AIG10 1 km borehole drilled in the early 2000 at the base of the Aigion fault scarp, and the 40–45° typical of the faults of the Corinth rift at intermediate depth in the brittle crust. A series of tests with hypothesis of 50°, 55°, and 60° favors he 60° case which gives residuals significantly lower (Figure 19), a value consistent with those proposed by Bernard et al. (2006) for the intermediate and shallow faults in that area. The parameters of our best fitting model are listed in Table 7 and the data, model, and fit are plotted in Figure 20. The RMS fit is at 0.5 mm. The uncertainties are deduced from the variation range measured thanks to the exploration of the domain of solutions (as in Figure 19 for all the parameters). For the best fitting solution, diagrams of the RMS versus length, width, slip, depth of upper tip, and azimuth, as well as depth versus length and slip versus length were used. Figure 21 shows the postseismic model in the cross section D-D′ (Figure 16) together with the projection of the 1995 fault and the recent seismicity from the catalogs distributed by the Corinth Rift Laboratory (CRL) observatory (http://catalogs.crlab.eu).

12.4. Discussion of the Model

Figure 22 shows the evolution of the seismic moment release inferred from our model. For the coseismic we take the seismic moment of Bernard et al. (1997), 390 10^{16} N m. This moment corresponds to the parameters that are reminded in Table 7 when assuming a rigidity of 3.3 10^{10} N m^{-2}. For the postseismic fault, as it is located at shallower, we used a value slightly lower, 2.7 10^{10} N m^{-2}, to calculate the plot of Figure 22. We see that, between 2002 and 2010, there was still a significant amount of moment release while after 2010 the modeled postseismic process is almost terminated. The cumulated seismic moment of the postseismic process represents 110 10^{16} N m, thus 28% of the coseismic or 22% of the whole sequence. Translated in equivalent magnitude, this model indicates that the postseismic process that took place mainly in the 15 years following the main shock (e.g., 2.5 *T*), corresponds to an earthquake of M_w = 5.9.

The fault (or deforming zone) inferred from our modeling is not the upward continuation of the 1995 rupture. The almost complete lack of slip in the uppermost kilometers of the 1995 rupture is not recovered during the postseismic period. Not only our model does not predict that, but the InSAR data show that it cannot be the case. Thus, our data does not bring new information for a better understanding of how and when the

deformation in the uppermost layers above the 1995 will occur (or has occurred). What our model suggest clearly instead is that

(a) there is an existing postseismic activity in the 15 years following the 1995 earthquake (best fitting decay time $T = 6$ years);
(b) that activity does not occur in the upward continuation of the 1995 rupture;
(c) instead, it occurs immediately west of the 1995 rupture along length of 7 km, thus twice shorter that the coseismic;
(d) it occurs at shallower depth than the coseismic, but not at very shallow depth, with a tip of the fault (or deforming zone) at ~1 km, that is, ~1.5 km if we apply the correction suggested by Cattin et al. (1999) to account for the low rigidity of the uppermost crust in the Corinth rift, and a bottom at ~6.5 km, thus a centroid at ~4 km depth.

During the period 1995–2010, the seismicity has been very well recorded in the rift of the Corinth, by the CRL Observatory (http://crlab.eu), and is has been observed a seismicity much stronger west of the 1995 fault than within the area of the 1995 fault. This microseismicity is very variable with time with clusters in time and space that have been studied in detail by various authors, for example, Lambotte et al. (2014). For the year 2006 for example the seismicity of the year is plotted at http://seismicity2006.crlab.eu (download catalogue from the CRL portal), and a dense cluster of seismicity can be seen near the lower end of our modeled deforming zone.

13. Conclusions

Using a multitemporal combination of ascending and descending PS and SBAS interferograms, coupled with velocities at a 73 GPS points, we produced maps of vertical and east-west velocities in the western rift of Corinth valid for the period 2002–2010. The coherence is good enough to give very accurate information in many areas. We produced a first set (S1) of vertical velocities with average accuracy below 1 mm/year at 4,391 points distributed across the entire area and a set (S2) of 951 vertical velocities with accuracy of ~0.5 mm/year, and more robust against unwrapping errors. We believe that the S2 set can be useful for several applications in geology, geophysics, and also for land use in urban and cultivated areas and in the river delta that are unconsolidated and weaker areas.

We believe that in many places those 2002–2010 velocities are not representing a long terms steady vertical velocity but they are a *picture* of the situation at a given epoch. Indeed,

(a) in the urban areas, the deformations (mainly subsidence, but it can uplift is some cases) can change with time because of the evolution of the activity, the use of the aquifers, and the climatic variability over periods of a few years;
(b) in the deltas temporal changes can occur and we already have such observation in the Mornos delta where the recent years are characterized by uplift (2 mm/year) in the place that was subsiding quickly (9 mm/year) 10 years before;
(c) in places affected by earthquakes, like Aigion, we found strong evidence for a postseismic signal, that we can model and discuss at the light of the know characteristics of the main event, and there are other places affected by transients like the area of the 2010 Efpalio earthquakes, or that of the 2008 Movri earthquake, that may have signatures in InSAR and GPS;
(d) although our 2002–2010 data set does not allow us to investigate temporal changes of the shallow slow slipping on the Rio-Patras fault, the combined analysis of ERS, ENVISAT, and SENTINEL might bring new insights in the future.

The city of Patras is well mapped with InSAR. Several discontinuities are obvious, some of them corresponding to discontinuities that were activated in the small and shallow earthquake of 1989. Those local discontinuities in the city are oblique with respect to the main tectonic structure of the area, the Rio-Patras, and might have a shallow hydro-geological origin rather than tectonic origin. The Rio-Patras fault is offshore, in front of downtown Patras and penetrates inland between Patras and Rio. Then it rotates progressively and connects with the Psathopyrgos normal fault at the entrance to the Corinth rift. The deformation shape of the Rio-Patras fault indicates a shallow locking depth and suggests slow slipping below that depth. The large gradient of strike-slip velocities between the south and the north coast at both ends of the Rio-Antirio bridge support a model of deformation accumulation in a very narrow locked layer in the crust, with the rest being

unlocked, and therefore not associated with strong seismicity (at least in the last decades until present). There might well be alternative models, for example, models invoking a low angle decollement at some depth in the crust, presumably 8–10 km if it is of the same nature of the one assumed at base of the Psathopyrgos fault (Duverger et al., 2018). Here we have not reviewed the other possible models nor investigated any of them, focusing our approach on the questions/answers that simple crack models in elastic media can answer. Even inexact models can have virtues when, manipulated as a deus ex machine, they permit to constraining some of the characteristics of the processes.

We found an uplift signal at Aigion that we modeled as a postseismic process. More work is needed, in particular the predictions of our model should be confronted more carefully to existing GPS data and to possible observations of vertical change in the Aigion harbor. We believe that the Selinous river delta, near Aigion, is not subsiding, or very little, due to the balance between the subsidence as a result of sediments compaction and the uplift due to offshore north dipping faults in the north being in equilibrium. Again, more observation at this location and comparison with the velocities in the ERS period (1992–2000) and Sentinel period (2014–present) could be great teacher. Several faults are located close to or inside river deltas where the observed vertical velocities mix compaction in the delta and tectonic motion across the fault, we developed methodologies to separate those effects. Finally, local deforming zones are mapped by InSAR near the cities of Nafpaktos, Akrata, Selianitika, Psathopyrgos, Psaromita, and at Trizonia Island, where we measured a ~0.8 μrad per year NW-SE tilt of the island.

Acknowledgments
We thank all the CRL team which participates every year to campaign field work to acquire a set of useful measurements enriching the GPS time series. We thank the French National Research Agency which, in the framework of *Hazard, seismogenic dynamics, and seismic/aseismic coupling of an active fault system in the western Rift of Corinth, Greece (SISCOR)* project, supported the current research. Moreover, the CRL (Corinth Rift Laboratory) fault vectors that have been used in the map of the current study are from this project and were compiled by N. Meyer. We acknowledge the European Space Agency for providing us with SAR data from ASAR/ENVISAT (ESA AOE766). We acknowledge KTIMATOLOGIO S.A. for kindly providing the digital elevation model. Most of the figures were obtained by employing the GMT freeware package by Wessel et al. (2013). The GPS solutions, continuous and campaign used in this study, shown in Tables 1 and 4 of Briole et al. (2000), have been updated and the vectors and their sigma values are provided in the supporting information. Special thanks to Gareth Carter for proofreading the manuscript for English language. Additionally, we acknowledge (in alphabetic order): Vassilis Anastassopoulos, Pascal Bernard, Nicolas Chamot-Rooke, Hélène Lyon-Caen, Issaak Parcharidis, Daniel Raucoules, Alexis Rigo, Michel Sebrier, Efthimios Sokos, and Christophe Vigny for their valuable comments, support, and discussions. RINEX files of the permanent and campaign points of the CRL can be found at http://crlab.eu. The best constrained version of the combined multitemporal InSAR data sets are included in the paper as supporting information, having a doi:10.5281/zenodo.1205496.

References

Athanasopoulos, G. A., & Leonidou, E. A. (1996). Effects of earthquake fault rupture propagation on nearby structures. *Transactions on the Built Environment*, *20*. https://doi.org/10.2495/ERES960081

Avallone, A. (2003*)*. Analyse de dix ans de déformation du rift de Corinthe (Grèce) par géodésie spatiale (Doctoral dissertation). Retrieved from Institut de Physique du Globe de Paris, France. https://www.theses.fr/2003GLOB0015

Avallone, A., Briole, P., Agatza-Balodimou, A. M., Billiris, H., Charade, O., Mitsakaki, C. A., et al. (2004). Analysis of eleven years of deformation measured by GPS in the Corinth Rift Laboratory area. *Comptes Rendus Geoscience*, *336*, 301–311. https://doi.org/10.1016/j.crte.2003.12.007

Baker, C., Hatzfeld, D., Lyon-Caen, H., Papadimitriou, E., & Rigo, A. (1997). Earthquake mechanisms of the Adriatic Sea and western Greece. *Geophysical Journal International*, *131*(3), 559–594. https://doi.org/10.1111/j.1365-246X.1997.tb06600.x

Bell, R. E., McNeill, L. C., Bull, J. M., & Henstock, T. J. (2008). Evolution of the offshore western Gulf of Corinth. *Geological Society of America Bulletin*, *120*(1–2), 156–178. https://doi.org/10.1130/B26212.1

Berardino, P., Fornaro, G., Lanari, R., & Sansosti, E. (2002). A new algorithm for surface deformation monitoring based on small baseline differential SAR interferograms. *IEEE Transactions on Geoscience and Remote Sensing*, *40*(11), 2375–2383. https://doi.org/10.1109/TGRS.2002.803792

Bernard, P., Briole, P., Meyer, B., Lyon-Caen, H., Gomez, J.-M., Tiberi, C., et al. (1997). The Ms = 6.2, June 15, 1995 Aigion earthquake (Greece): Evidence for low angle normal faulting in the Corinth rift. *Journal of Seismology*, *1*(2), 131–150. https://doi.org/10.1023/A:1009795618839

Bernard, P., Lyon-Caen, H., Briole, P., Deschamps, A., Boudin, F., Makropoulos, K., et al. (2006). Seismicity, deformation and seismic hazard in the western rift of Corinth: New insights from the Corinth Rift Laboratory (CRL). *Tectonophysics*, *426*(1–2), 7–30. https://doi.org/10.1016/j.tecto.2006.02.012

Braunmiller, J., & Nábělek, J. (1996). Geometry of continental normal faults: Seismological constraints. *Journal of Geophysical Reseach*, *101*(B2), 3045–3052. https://doi.org/10.1029/95JB02882

Briole, P. (2017). Modelling of earthquake slip by inversion of GNSS and InSAR data assuming homogenous elastic medium. *Zenodo*. https://doi.org/10.5281/zenodo.1098399

Briole, P., De Natale, G., Gaulon, R., Pingue, F., & Scarpa, R. (1986). Inversion of geodetic data and seismicity associated with the Friuli earthquake sequence (1976–1977). *Annales Geophysicae*, *4*(4), 481–492.

Briole, P., Rigo, A., Lyon-Caen, H., Ruegg, J. C., Papazissi, K., Mitsataki, C., et al. (2000). Active deformation of the Corinth rift, Greece: Results from repeated Global Positioning System surveys between 1990 and 1995. *Journal of Geophysical Research*, *105*(B11), 25,605–25,625. https://doi.org/10.1029/2000JB900148

Casu, F., Manzo, M., & Lanari, R. (2006). A quantitative assessment of the SBAS algorithm performance for surface deformation retrieval from DInSAR data. *Remote Sensing of Environment*, *102*(3–4), 195–210. https://doi.org/10.1016/j.rse.2006.01.023

Cattin, R., Briole, P., Lyon-Caen, H., Bernard, P., & Pinettes, P. (1999). Effects of superficial layers on coseismic displacements for a dip-slip fault and geophysical implications. *Geophysical Journal International*, *137*(1), 149–158. https://doi.org/10.1046/j.1365-246x.1999.00779.x

Clarke, P., Davies, R., England, P., Parsons, B., Billiris, H., Paradissis, D., et al. (1997). Geodetic estimate of seismic hazard in the Gulf of Korinthos. *Geophysical Research Letters*, *24*(11), 1303–1306. https://doi.org/10.1029/97GL01042

Console, R., Falcone, G., Karakostas, V., Murru, M., Papadimitriou, E., & Rhoades, D. (2013). Renewal models and coseismic stress transfer in the Corinth Gulf, Greece, fault system. *Journal of Geophysical Research: Solid Earth*, *118*, 3655–3673. https://doi.org/10.1002/jgrb.50277

Cornet, F., & Bourouis S. (2013). High frequency monitoring of the Aigion fault activity. *Geophysical Reseach Abstracts*. Vol. 15, EGU2013–3306-5. Presented at European Geosciences Union General Assembly 12–17 April, 2015, Vienna, Austria.

De Martini, P. M., Pantosti, D., Palyvos, N., Lemeille, F., McNeill, L., & Collier, R. (2004). Slip rates of the Aigion and Eliki faults from uplifted marine terraces, Corinth Gulf, Greece. *Comptes Rendus Geoscience*, *336*(4–5), 325–334. https://doi.org/10.1016/j.crte.2003.12.006

Doan, M. L., & Cornet, F. H. (2007). Thermal anomaly near the Aigio fault, Gulf of Corinth, Greece, maybe due to convection below the fault. *Geophysical Research Letters*, *34*, L06314. https://doi.org/10.1029/2006GL028931

Doutsos, T., & Poulimenos, G. (1992). Geometry and kinematics of active faults and their seismotectonic significance in the western Corinth-Patras Rift (Greece). *Journal of Structural Geology*, *14*(6), 689–699. https://doi.org/10.1016/0191-8141(92)90126-H

Duverger, C., Godano, M., Bernard, P., Lyon-Caen, H., & Lambotte, S. (2015). The 2003–2004 seismic swarm in the western Corinth rift: Evidence for a multiscale pore pressure diffusion process along a permeable fault system. *Geophysical Research Letters*, *42*, 7374–7382. https://doi.org/10.1002/2015GL065298

Duverger, C., Lambotte, S., Bernard, P., Lyon-Caen, H., Deschamps, A., & Nercessian, A. (2018). Dynamics of microseismicity and its relationship with the active structures in the western Corinth rift (Greece). *Geophysical Journal International*, *215*(1), 196–221. https://doi.org/10.1093/gji/ggy264

Ferretti, A., Prati, C., & Rocca, F. (2000). Nonlinear subsidence rate estimation using permanent scatterers in differential SAR Interferometry. *IEEE Transactions on Geoscience and Remote Sensing*, *38*(5), 2202–2212. https://doi.org/10.1109/36.868878

Ferretti, A., Prati, C., & Rocca, F. (2001). Permanent Scatterers in SAR Interferometry. *IEEE Transactions on Geoscience and Remote Sensing*, *39*(1), 8–20. https://doi.org/10.1109/36.898661

Flotte, N., Sorela, D., Mullerm, C., & Tensic, J. (2005). Along strike changes in the structural evolution over a brittle detachment fault: Example of the Pleistocene Corinth-Patras rift (Greece). *Tectonophysics*, *403*(1–4), 77–94. https://doi.org/10.1016/j.tecto.2005.03.015

Ford, M., Williams, E. A., Malartre, F., Popescu, S. M., & Nichols, G. (2007). Stratigraphic architecture, sedimentology and structure of the Vouraikos Gilbert-type fan delta, Gulf of Corinth, Greece. *Sedimentary Processes, Environments and Basins: A Tribute to Peter Friend*, *38*, 49–90.

Hatzfeld, D., Kementzetzidou, D., Karakostas, V., Ziazia, M., Nothard, S., Diagourtas, D., et al. (1996). The Galaxidi earthquake of 18 November 1992: A possible asperity within the normal fault system of the Gulf of Corinth (Greece). *Bulletin of the Seismological Society of America*, *86*, 1987–1991.

Hooper, A. (2008). A multi-temporal InSAR method incorporating both persistent scatterer and small baseline approaches. *Geophysical Research Letters*, *35*, L16302. https://doi.org/10.1029/2008GL034654

Hooper, A., Segall, P., & Zebker, H. (2007). Persistent scatterer InSAR for crustal deformation analysis, with application to Volcán Alcedo, Galápagos. *Journal of Geophysical Research*, *112*, B07407. https://doi.org/10.1029/2006JB004763

Hooper, A., Zebker, H., Segall, P., & Kampes, B. (2004). A new method for measuring deformation on volcanoes and other natural terrains using InSAR persistent scatterers. *Geophysical Research Letters*, *31*, L23611. https://doi.org/10.1029/2004GL021737

Kalteziotis, N., Sabatakakis, N., Koukis, G., Zervogiannis, H., & Tsiambaos G. (1991). Structural damage in a populated area due to an active fault. Paper presented at International Conference on Recent Advances in Geotechnical Earthquake Engineering and Soil Dynamics, March 11-15, 1991, St. Louis, Missouri, Paper no LP28. http://scholarsmine.mst.edu/icrageesd/02icrageesd/session13/17

Kampes, B., Hanssen, R., & Perski Z. (2003). Radar interferometry with public domain tools. Paper presented at 3rd International Workshop on ERS SAR Interferometry, FRINGE03, Frascati, Italy, 1-5 Dec 2003, page 6. http://doris.tudelft.nl/Literature/kampes03b.pdf

Kampes, B. M. (2005). Displacement parameter estimation using permanent scatterer interferometry (Doctoral dissertation). Retrieved from Delft University of Technology, Holland. https://www.narcis.nl/publication/RecordID/oai:tudelft.nl:uuid:9f11f2ef-2db4-4583-a763-aee88e06ee3b

Kiratzi, A., & Louvari, E. (2003). Focal mechanisms of shallow earthquakes in the Aegean Sea and the surrounding lands determined by waveform modelling: A new database. *Journal of Geodynamics*, *36*(1–2), 251–274. https://doi.org/10.1016/S0264-3707(03)00050-4

Koukis, G., Sabatakakis, N., Tsiambaos, G., & Katrivesis, N. (2005). Engineering geological approach to the evaluation of seismic risk in metropolitan regions: Case study of Patras, Greece. *Bulletin of Engineering Geology and the Environment*, *64*(3), 219–235. https://doi.org/10.1007/s10064-005-0273-x

Koukouvelas, I., Asimakopoulos, M., & Doutsos, T. (1999). Fractal characteristics of active normal faults: An example of the eastern Gulf of Corinth, Greece. *Tectonophysics*, *308*(1–2), 263–274. https://doi.org/10.1016/S0040-1951(99)00087-6

Lambotte, S., Lyon-Caen, H., Bernard, P., Deschamps, A., Patau, G., Nercessian, A., et al. (2014). Reassessment of the rifting process in the Western Corinth Rift from relocated seismicity. *Geophysical Journal International*, *197*(3), 1822–1844. https://doi.org/10.1093/gji/ggu096

Liotier, Y., (1989). Modélisation des ondes de volume des séismes de l'arc Ageen (maste's thesis). Retrieved from Université Joseph Fourier, Grenoble, France.

Lykousis, V., Sakellariou, D., Moretti, I., & Kaberi, H. (2007). Late Quaternary basin evolution of the Gulf of Corinth: Sequence stratigraphy, sedimentation, fault-slip and subsidence rates. *Tectonophysics*, *440*(1–4), 29–51. https://doi.org/10.1016/j.tecto.2006.11.007

McNeill, L. C., Cotterill, C. J., Bull, J. M., Henstock, T. J., Bell, R., & Stefatos, A. (2007). Geometry and slip rate of the Aigion fault, a young normal fault system in the western Gulf of Corinth. *Geology*, *35*(4), 355–358. https://doi.org/10.1130/G23281A.1

Moretti, I., Lykousis, V., Sakellariou, D., Reynaud, J. Y., Benziane, B., & Prinzhoffer, A. (2004). Sedimentation and subsidence rate in the Gulf of Corinth: What we learn from the Marion Dufresne's long-piston coring. *Comptes Rendus Geoscience*, *336*(4–5), 291–299. https://doi.org/10.1016/j.crte.2003.11.011

Moretti, I., Sakellariou, D., Lykousis, V., & Micarelli, L. (2003). The Gulf of Corinth: An active half graben? *Journal of Geodynamics*, *36*(1–2), 323–340. https://doi.org/10.1016/S0264-3707(03)00053-X

Müller, M. D., Geiger, A., Kahle, H.-G., Veis, G., Billiris, H., Paradissis, D., & Felekis, S. (2011). Velocity and deformation fields in the North Aegean domain, Greece, and implications for fault kinematics, derived from GPS data 1993–2009. *Tectonophysics*, *597-598*, 34–49. https://doi.org/10.1016/j.tecto.2012.08.003

Okada, Y. (1992). Internal deformation due to shear and tensile faults in a half-space. *Bulletin of the Seismological Society of America*, *82*, 1018–1040.

Palyvos, N., Pantosti, D., De Martini, P. M., Lemeille, F., Sorel, D., & Pavlopulos, K. (2005). The Aigion-Neos Erineos coastal normal fault system (western Corinth Gulf rift, Greece): Geomorphological signature, recent earthquake history, and evolution. *Journal of Geophysical Research*, *110*, B09302. https://doi.org/10.1029/2004JB003165

Palyvos, N., Pantosti, D., Stamatopoulos, L., & De Martini, P. M. (2007). Geomorphological reconnaissance of the Psathopyrgos and Rion-Patras fault zones (Achaia, NW Peloponnesus). *Bulletin of the Geological Society of Greece*, *40*, 1586–1598. https://doi.org/10.12681/bgsg.17063

Pantosti, D., De Martini, P. M., Koukouvelas, I., Stamatopoulos, L., Palyvos, N., Pucci, S., et al. (2004). Palaeoseismological investigations of the Aigion Fault (Gulf of Corinth, Greece). *Comptes Rendus Geoscience*, *336*(4–5), 335–342. https://doi.org/10.1016/j.crte.2003.12.005

Papazachos, B. C. (1975). Seismic activity along the Saronikos–Corinth–Patras gulfs. Monthly Bulletin of the Seismological Institute of the National Observatory of Athens, 1-16.

Parcharidis, I., Kokkalas, S., Fountoulis, I., & Foumelis, M. (2009). Detection and monitoring of active faults in urban environments: Time series interferometry on the cities of Patras and Pyrgos (Peloponnese, Greece). *Remote Sensing*, *1*(4), 676–696. https://doi.org/10.3390/rs1040676

Parcharidis, I., Kourkouli, P., Karymbalis, E., Foumelis, M., & Karathanassi, V. (2013). Time series synthetic aperture radar interferometry for ground deformation monitoring over a small scale tectonically active deltaic environment (Mornos, Central Greece). *Journal of Coastal Research*, *287*(2), 325–338. https://doi.org/10.2112/JCOASTRES-D-11-00106.1

Piper, D., Kontopoulos, N., Anagnostou, C., Chronis, G., & Panagos, A. G. (1990). Modern fan deltas in the western Gulf of Corinth, Greece. *Geo-Marine Letters*, *10*(1), 5–12. https://doi.org/10.1007/BF02431016

Rohais, S., Eschard, R., & Guillocheau, F. (2008). Depositional model and stratigraphic architecture of rift climax Gilbert-type fan deltas (Gulf of Corinth, Greece). *Sedimentary Geology*, *210*(3–4), 132–145. https://doi.org/10.1016/j.sedgeo.2008.08.001

Schmidt, D. A., & Bürgmann, R. (2003). Time-dependent land uplift and subsidence in the Santa Clara valley, California, from a large interferometric synthetic aperture radar data set. *Journal of Geophysical Research*, *108*(B9), 2416. https://doi.org/10.1029/2002JB002267

Serpetsidaki, A., Elias, P., Ilieva, M., Bernard, P., Briole, P., Deschamps, A., et al. (2014). New constraints from seismology and geodesy on the Mw=6.4 2008 Movri (Greece) earthquake. Evidence for a growing strike-slip fault system. *Geophysical Journal International*, *198*(3), 1373–1386. https://doi.org/10.1093/gji/ggu212

Sokos, E., Zahradnik, J., Kiratzi, A., Jansky, J., Gallovic, F., Novotny, O., et al. (2012). The January 2010 Efpalio earthquake sequence in the western Corinth Gulf (Greece). *Tectonophysics*, *530-531*, 299–309. https://doi.org/10.1016/j.tecto.2012.01.005

Soter, S., & Katsonopoulou, D. (1999). Occupation horizons found in the search for the ancient Greek City of Helike. *Geoarchaeology*, *14*(6), 531–563. https://doi.org/10.1002/(SICI)1520-6548(199908)14:6<531::AID-GEA4>3.0.CO;2-X

Stamatopoulos, L., Kontopoulos, N., Voltaggio, M., & Branca, M. (2004). Radiochronological data with U/Th method in lagoonal/marine deposits of the NW Peloponnese, Greece. *Bulletin of the Geological Society of Greece*, *36*, 1064–1067.

Tarantola, A., & Valette, B. (1982). Generalized nonlinear inverse problems solved using the least squares criterion. *Reviews of Geophysics*, *20*(2), 219–232. https://doi.org/10.1029/RG020i002p00219

Taymaz, T., Jackson, J., & McKenzie, D. (1991). Active tectonics of the north and central Aegean Sea. *Geophysical Journal International*, *106*(2), 433–490. https://doi.org/10.1111/j.1365-246X.1991.tb03906.x

Van der Kooij, M., Hughes, W., Sato, S., & Poncos, V. (2005). Coherent target monitoring at high spatial density: Examples of validation results. *Proceedings of the Fringe 2005, ESA*.

Wessel, P., Smith, W. H. F., Scharroo, R., Luis, J. F., & Wobbe, F. (2013). GMT 5: A major new release of the Generic Mapping Tools. *Eos, Transactions of the American Geophysical Union*, *94*(45), 409–410. https://doi.org/10.1002/2013EO450001